Biomech Model Mechanobiol
DOI 10.1007/s10237-014-0619-z

ORIGINAL PAPER

Modeling function–perfusion behavior in liver lobules including tissue, blood, glucose, lactate and glycogen by use of a coupled two-scale PDE–ODE approach

T. Ricken · D. Werner · H. G. Holzhütter · M. König · U. Dahmen · O. Dirsch

Received: 6 February 2014 / Accepted: 2 September 2014

Abstract This study focuses on a two-scale, continuum multicomponent model for the description of blood perfusion and cell metabolism in the liver. The model accounts for a spatial and time depending hydro-diffusion–advection–reaction description. We consider a solid-phase (tissue) containing glycogen and a fluid-phase (blood) containing glucose as well as lactate. The five-component model is enhanced by a two-scale approach including a macroscale (sinusoidal level) and a microscale (cell level). The perfusion on the macroscale within the lobules is described by a homogenized multiphasic approach based on the theory of porous media (mixture theory combined with the concept of volume fraction). On macro level, we recall the basic mixture model, the governing equations as well as the constitutive framework including the solid (tissue) stress, blood pressure and solutes chemical potential. In view of the transport phenomena, we discuss the blood flow including transverse isotropic permeability, as well as the transport of solute concentrations including diffusion and advection. The continuum multicomponent model on the macroscale finally leads to a coupled system of partial differential equations (PDE). In contrast, the hepatic metabolism on the microscale (cell level) was modeled via a coupled system of ordinary differential equations (ODE). Again, we recall the constitutive relations for cell metabolism level. A finite element implementation of this framework is used to provide an illustrative example, describing the spatial and time-depending perfusion–metabolism processes in liver lobules that integrates perfusion and metabolism of the liver.

Keywords Multi phase · Multi component · Two scale · Liver tissue · Liver perfusion · Sinusoidal perfusion · Hydro-diffusion–advection-reaction model · Cell metabolism · Coupled problem · Porous media

1 Introduction

The liver is a vital organ in vertebrates and plays a key metabolic role for the whole body. Main metabolic functions are among others detoxification, protein synthesis and metabolic homeostasis. A central task of the liver is the homeostasis of the blood glucose within a range of maximal 9 mM after food intake and minimal values of around 3mM after fasting and exercise. The liver is crucial for glucose regulation due to its ability (i) to store glucose in its storage form glycogen and (ii) to switch between hepatic glucose production (HGP) when glucose is low (hypoglycemia)

T. Ricken (✉) · D. Werner
Institute of Mechanics, Structural Analysis and Dynamics, TU Dortmund University, August-Schmidt-Str. 6,
44227 Dortmund, Germany
e-mail: tim.ricken@tu-dortmund.de

D. Werner
e-mail: danielq.werner@tu-dortmund.de

H. G. Holzhütter · M. König
Institute of Biochemistry, University Medicine Charité Berlin,
Virchowweg 6, 10117 Berlin, Germany
e-mail: hergo@charite.de

M. König
e-mail: matthias.koenig@charite.de

U. Dahmen
Department of General, Visceral and Transplantation Surgery,
University Hospital Jena, Drackendorfer Str. 1, 07747 Jena,
Germany
e-mail: uta.dahmen@med.uni-jena.de

O. Dirsch
Insitute of Pathology, University Hospital Jena, Ziegelmühlenweg 1,
07747 Jena, Germany
e-mail: olaf.dirsch@med.uni-jena.de

and hepatic glucose utilization (HGU) when glucose is high (hyperglycemia) (Gerich 1993; König et al. 2012).

The glucose produced by the liver originates either from de novo glucose synthesis from precursors like lactate, a process called gluconeogenesis, or it is released from glycogen (glycogenolysis). On the other hand, glucose utilized by the liver either can be stored as glycogen (glycogen synthesis) or be used for energy production in glycolysis. Glucose homeostasis is controlled by several hormones, with insulin and glucagon being the main counteracting players. Insulin lowers blood glucose, whereas glucagon raises glucose levels, and therefore plays an important role in counterregulation to hypoglycemia. The effect of these hormones is due to the activation of signaling cascades in the target organs, consequently resulting in adaptation of metabolic pathways.

Hepatocytes, the main cell type of the liver, are the central place of metabolism. Hepatocytes are arranged in hexagonal functional segments, called liver lobules. The liver lobules are arranged in lattice, see Fig. 1. Each corner of the hexagonal lobule harbors the so-called portal triad which is formed by the bile duct collecting the bile fluid produced by the hepatocytes, an artery ensuring the supply of oxygen enriched systemic blood and a portal vein delivering nutrient-rich blood from the digestive organs, see Fig. 2. In the center of each lobule, the central vein drains the blood coming from the portal triad. The numerous capillaries connecting the peri-portal blood vessels of the portal triad with the central vein are called sinusoids. They are flanked by columns of tightly connected hepatocytes. This liver-specific arrangement of blood vessels entails an anisotropic blood flow in the liver lobules.

The geometry and local density of sinusoids in a liver lobule may considerably vary in a seemingly erratic manner (see Fig. 4) thus making it all but impossible to model microcirculation based on an accurate discrete geometrical description of the sinusoidal network. Therefore, an attractive alternative is to apply multiphasic mixture theory based on the theory of porous media (TPM); see de Boer (1996, 2000) and Ehlers (2002). The main difference of the TPM to other multiphasic theories, such as the mixture theory, cf. Bowen (1976a), Truesdell and Toupin (1960), Mow et al. (1989), Lai et al. (1991) or Biot's theory, cf. Biot (1935, 1941), is the introduction of the constitutive framework; see de Boer (1996), de Boer (2000) or Lu and Hanyga (2005).

The presented investigation is based on the liver perfusion model given in Ricken et al. (2010). Alternative liver perfusion models can be found in Debbaut et al. (2014) or Siggers et al. (2014).

In this contribution, we focus on the interaction between liver blood perfusion and cell metabolism. Moreover, remodeling aspects with respect to a change in the microperfusion direction are also considered, see Sect. 4.1.

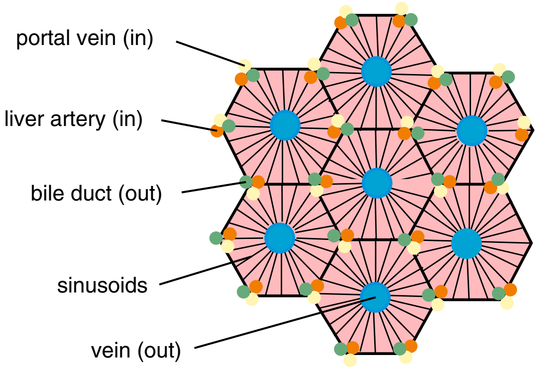

Fig. 1 Structure of a lattice of liver lobules

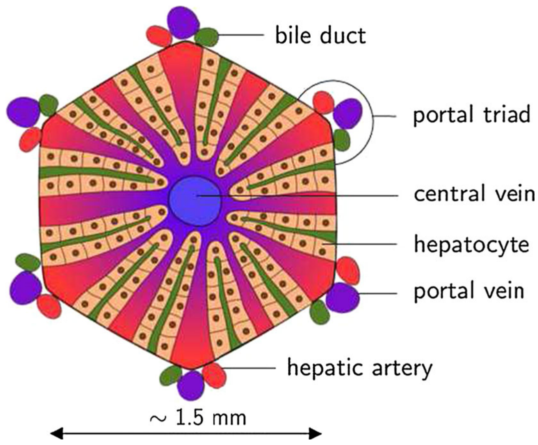

Fig. 2 Structure of one liver lobule

2 Basic liver model on microperfusion level

From a more biomechanical point of view, the components of soft biological tissues show a high similarity among each other. Generally, they consist of two phases, namely a porous solid body (solid phase) saturated with fluids (fluid phase), e.g. blood, lymph or bile. For the macroscopic lobule level, a continuum mechanical, multiphasic formulation to describe the anisotropic blood flow will be presented. For the microscopic level, we present an embedded set of ordinary differential equations describing the hepatic metabolism. Different scales are depicted in Fig. 3.

2.1 Mixture body

The considered porous body φ consists of $\boldsymbol{\kappa} = \mathbf{2}$ phases $\varphi^{\boldsymbol{\alpha}}$, namely a solid $\varphi^{\mathbf{S}}$ and a fluid $\varphi^{\mathbf{F}}$ ($\boldsymbol{\alpha} \in \{\mathbf{S}, \mathbf{F}\}$). Both phases are considered as mutually immiscible materials that are heterogeneously composed. For the representation of phase $\varphi^{\boldsymbol{\alpha}}$ including miscible substances, we follow the classical mixture theory, cf. Bowen (1976b), Greve (2003), Hutter and Jöhnk (2004). Therefore, we split each immiscible phases $\varphi^{\boldsymbol{\alpha}}$ into ν components, namely into one carrier phase φ^{α},

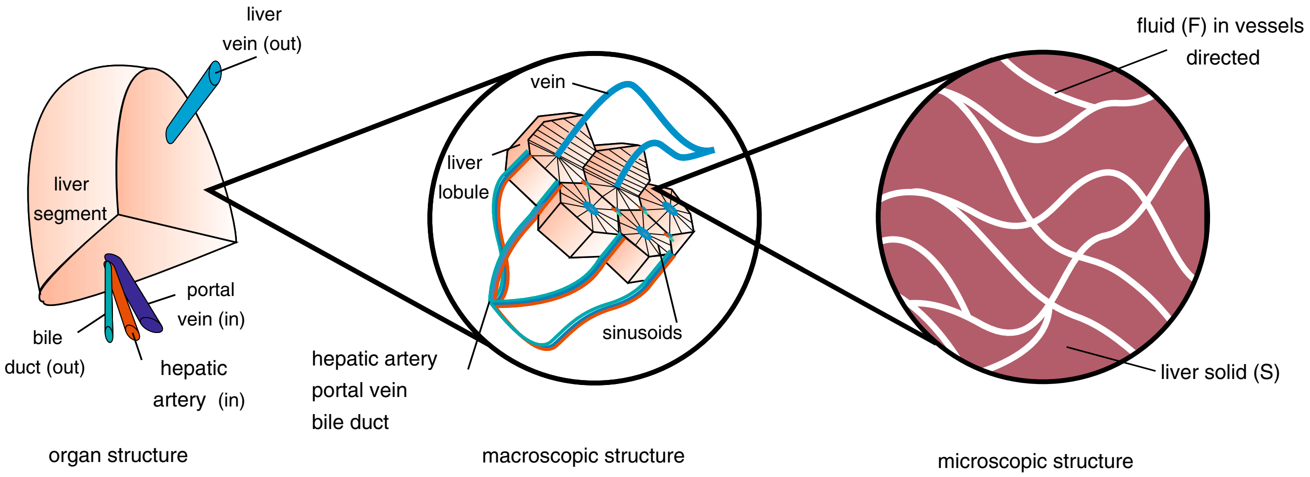

Fig. 3 Macro (liver, lobes and segments), meso (lobule) and microstructure (microcirculation in sinusoids) of the liver

called solvent and $\mu = \nu - 1$ miscible substances $\varphi^{\alpha\beta}$, called solutes. To be more general, by default, all miscible substances $\varphi^{\alpha\beta}$ can exist in each solvent φ^{α}. Consequently, $\pi = (\mu + 1)\,\kappa = \nu\,\kappa$ denotes the maximum number of possible components. Thus, the composition of the considered body φ can be expressed via

$$\varphi = \sum_{\boldsymbol{\alpha}=1}^{\kappa} \varphi^{\boldsymbol{\alpha}} = \sum_{\alpha=1}^{\kappa} \left[\varphi^{\alpha} + \sum_{\beta=1}^{\nu-1} \varphi^{\alpha\beta} \right]. \tag{1}$$

2.2 Volume fractions and concentrations

The overall volume of the whole mixture is denoted by dv, the partial volume of the phase $\varphi^{\boldsymbol{\alpha}}$ by $\mathrm{dv}^{\boldsymbol{\alpha}}$ and the volume of the main carrier phase φ^{α} by dv^{α}. If the impact of a solute $\varphi^{\alpha\beta}$ on the phase volume $\mathrm{dv}^{\boldsymbol{\alpha}}$ of the solvent φ^{α} is insignificantly small, the assumption holds that the volume of the phase $\varphi^{\boldsymbol{\alpha}}$ is nearly equivalent to the volume of the carrier phase φ^{α}, i.e., the simplification

$$\mathrm{dv}^{\alpha} = \mathrm{dv}^{\boldsymbol{\alpha}} \tag{2}$$

is reasonable and will be presumed in the following contribution. Although the volume of overall phase $\varphi^{\boldsymbol{\alpha}}$ is set to be independent of the solute $\varphi^{\alpha\beta}$, it must be pointed out that the mass of the phase $\varphi^{\boldsymbol{\alpha}}$ will be influenced by the solute $\varphi^{\alpha\beta}$ since the partial molar density $\rho^{\alpha\beta}$ stays a function of the solvent molar concentration $\mathrm{c}^{\alpha\beta}$, see Eq. (12). A detailed description of the used kinematics is given in the "Kinematics" section of Appendix.

To account for the contribution of different phases, solvents or solutes in a mixture, a natural and convenient variable is the concentration which can be expressed in different ways:

- volume fraction (also volume concentration):

  $$\mathrm{n}^{\alpha} = \frac{\mathrm{dv}^{\alpha}}{\mathrm{dv}}\,, \quad \text{Unit: } \left[\frac{\mathrm{m}^3}{\mathrm{m}^3}\right] = [-], \tag{3}$$

  ratio of the partial volume dv^{α} of one constituent to the overall volume dv.
- Partial density (also mass concentration on mixture volume basis):

  $$\rho^{\alpha} = \frac{\mathrm{dm}^{\alpha}}{\mathrm{dv}}\,, \quad \text{Unit: } \left[\frac{\mathrm{kg}}{\mathrm{m}^3}\right], \tag{4}$$

  ratio of the partial mass dm^{α} of one constituent to the overall mixture volume dv.
- True density (also mass concentration on constituent volume basis):

  $$\rho^{\alpha\mathrm{R}} = \frac{\mathrm{dm}^{\alpha}}{\mathrm{dv}^{\alpha}}\,, \quad \text{Unit: } \left[\frac{\mathrm{kg}}{\mathrm{m}^3}\right], \tag{5}$$

  ratio of the partial mass dm^{α} of one constituent to partial volume dv^{α} of that constituent.
- Mixture volume molar concentration:

  $$\mathrm{c}^{\beta} = \frac{\mathrm{dn}^{\beta}_{\mathrm{mol}}}{\mathrm{dv}}\,, \quad \text{Unit: } \left[\frac{\mathrm{mol}}{\mathrm{m}^3}\right], \tag{6}$$

  number of moles $\mathrm{dn}^{\beta}_{\mathrm{mol}}$ of a solute $\varphi^{\alpha\beta}$ in a solvent φ^{α} with respect to the overall mixture volume dv.
- Solvent volume molar concentration (also molarity of solute in a solution):

  $$\mathrm{c}^{\alpha\beta} = \frac{\mathrm{dn}^{\beta}_{\mathrm{mol}}}{\mathrm{dv}^{\alpha}}\,, \quad \text{Unit: } \left[\frac{\mathrm{mol}}{\mathrm{m}^3}\right], \tag{7}$$

  number of moles $\mathrm{dn}^{\beta}_{\mathrm{mol}}$ of a solute $\varphi^{\alpha\beta}$ in a solvent φ^{α} with respect to the solvent volume dv^{α}

The first three definitions are feasible to describe compositions of mutual immiscible components like fluid and tissue, whereas the latter two definitions are suitable for the description of solutions or molecules bound to the tissue. The mixture volume molar concentration c^{β} is adequate for modeling growth of solute content, cf. Ateshian et al. (2009), whereas the molarity of solute in a solution $\mathrm{c}^{\alpha\beta}$ is compatible with the common usage in chemistry and very feasible to describe chemical and biochemical reactions.

Here, we use the volume fraction n^{α}, as well as the partial and true density ρ^{α} and $\rho^{\alpha\mathrm{R}}$ for the description of the immiscible phases, whereas the miscible components are captured by the molar concentration $\mathrm{c}^{\alpha\beta}$ based on solvent volume. In view of the volume fractions, the saturation condition

$$\sum_{\boldsymbol{\alpha}}^{\mathbf{S},\mathbf{F}} \mathrm{n}^{\boldsymbol{\alpha}}(\mathbf{x},\mathrm{t}) \cong \sum_{\alpha}^{\mathrm{S},\mathrm{F}} \mathrm{n}^{\alpha}(\mathbf{x},\mathrm{t}) = \sum_{\alpha}^{\mathrm{S},\mathrm{F}} \frac{\rho^{\alpha}}{\rho^{\alpha\mathrm{R}}} = 1\,, \tag{8}$$

has to be fulfilled, where

$$\begin{aligned} &\mathrm{n}^{\boldsymbol{\alpha}} \cong \mathrm{n}^{\alpha} = \mathrm{n}^{\alpha}(\mathbf{x},\mathrm{t}), \quad \rho^{\alpha\mathrm{R}} = \rho^{\alpha\mathrm{R}}\,(\mathbf{x},\mathrm{t}),\\ &\rho^{\alpha} = \rho^{\alpha}(\mathbf{x},\mathrm{t}) = \mathrm{n}^{\alpha}\,\rho^{\alpha\mathrm{R}}, \end{aligned} \tag{9}$$

is considered with $\mathbf{x}$ as the position vector of the spatial point X in the actual placement and t as the time; see, e.g., de Boer (2000) and "Kinematics" section of Appendix. Due to the presumption made in (2), it must be pointed out that only volume fractions of the main carrier phases φ^{α} are considered in the saturation condition since the volume fractions of the solutes $\varphi^{\alpha\beta}$ are negligibly small.

The molecular weight of a constituent is given with the invariant

$$\mathrm{M}^{\beta}_{\mathrm{mol}} := \frac{\mathrm{dm}^{\beta}}{\mathrm{dn}^{\beta}_{\mathrm{mol}}}\left[\frac{\mathrm{g}}{\mathrm{mol}}\right], \tag{10}$$

which leads with

$$\mathrm{dm}^{\beta} = \mathrm{c}^{\alpha\beta}\,\mathrm{M}^{\beta}_{\mathrm{mol}}\,\mathrm{dv}^{\alpha} = \mathrm{n}^{\alpha}\,\mathrm{c}^{\alpha\beta}\,\mathrm{M}^{\beta}_{\mathrm{mol}}\,\mathrm{dv} =: \rho^{\alpha\beta}\,\mathrm{dv} \tag{11}$$

by using (3) to the definition of the partial molar density

$$\rho^{\alpha\beta} := \mathrm{n}^{\alpha}\,\mathrm{c}^{\alpha\beta}\,\mathrm{M}^{\beta}_{\mathrm{mol}}, \tag{12}$$

i.e., $\rho^{\alpha\beta}$ denotes the molar mass of the substance $\varphi^{\alpha\beta}$ with respect to the volume dv^{α} of the carrier phase φ^{α}. By evaluating the balance equation of mass for the concentrations (22), a supply of concentrations can also be expressed via

$$\hat{\mathrm{c}}^{\alpha\beta} = \frac{\hat{\rho}^{\alpha\beta}}{\mathrm{M}^{\beta}_{\mathrm{mol}}}\,, \tag{13}$$

whereas $\hat{\rho}^{\alpha\beta}$ denotes the mass supply terms within the balance equation of mass.

2.3 Balance equations and constraint conditions

The field equations for the investigated porous media contain the balance equations of the phases $\varphi^{\boldsymbol{\alpha}}$. We exclude additional supply terms of moment of momentum (nonpolar materials: supply terms of moment of momentum cannot be considered since these materials have no local rotational degrees of freedom). Thus, the balance equations for a saturated porous medium with respect to isothermal processes are given by the local statements of the balance equations of mass, momentum and moment of momentum via

$$\begin{aligned} &(\rho^{\boldsymbol{\alpha}})'_{\boldsymbol{\alpha}} + \rho^{\boldsymbol{\alpha}}\,\mathrm{div}\,\mathbf{x}'_{\boldsymbol{\alpha}} = \hat{\rho}^{\boldsymbol{\alpha}}\,,\\ &\mathrm{div}\,\mathbf{T}^{\boldsymbol{\alpha}} + \rho^{\boldsymbol{\alpha}}\,(\mathbf{b} - \mathbf{x}''_{\boldsymbol{\alpha}}) = \hat{\rho}^{\boldsymbol{\alpha}}\,\mathbf{x}'_{\boldsymbol{\alpha}} - \hat{\mathbf{p}}^{\boldsymbol{\alpha}}\,,\\ &\mathbf{T}^{\boldsymbol{\alpha}} = (\mathbf{T}^{\boldsymbol{\alpha}})^{\mathrm{T}}. \end{aligned} \tag{14}$$

In (14), "div" denotes the spatial divergence operator, $\mathbf{T}^{\boldsymbol{\alpha}}$ is the partial Cauchy stress tensor and $\rho^{\boldsymbol{\alpha}}\,\mathbf{b}$ specifies the volume force. The quantities $\hat{\rho}^{\boldsymbol{\alpha}}$ and $\hat{\mathbf{p}}^{\boldsymbol{\alpha}}$ represent the mass supply between the phases and the interaction forces of momentum of the constituents $\varphi^{\boldsymbol{\alpha}}$, respectively. In addition, $\hat{\rho}^{\boldsymbol{\alpha}}\,\mathbf{x}'_{\boldsymbol{\alpha}}$ specifies the moment resulting from the mass supply. Following the metaphysical principles of Truesdell (1984), the overall mixture body has to behave like a one component body which leads to the restrictions

$$\begin{aligned} &\sum_{\boldsymbol{\alpha}=1}^{\kappa} \hat{\rho}^{\boldsymbol{\alpha}} = \sum_{\alpha=1}^{\kappa}\left[\left(\sum_{\beta=1}^{\nu-1}\hat{\rho}^{\alpha\beta}\right) + \hat{\rho}^{\alpha}\right] = 0,\\ &\sum_{\boldsymbol{\alpha}=1}^{\kappa} \hat{\mathbf{p}}^{\boldsymbol{\alpha}} = \sum_{\alpha=1}^{\kappa}\left[\left(\sum_{\beta=1}^{\nu-1}\hat{\mathbf{p}}^{\alpha\beta}\right) + \hat{\mathbf{p}}^{\alpha}\right] = \mathbf{o}. \end{aligned} \tag{15}$$

3 Assumptions

In this contribution, we consider that the liver consists of two phases $\varphi^{\boldsymbol{\alpha}}$ with $\boldsymbol{\alpha} \in \{\mathbf{S}(\text{liver tissue}), \mathbf{F}(\text{blood})\}$. The liver tissue matrix $\varphi^{\mathbf{S}}$ is composed of the hyperelastic tissue matrix φ^{S} build of hepatocytes which include glycogen as an internal solute φ^{SGy}, whereas the fluid phase consists of blood φ^{F} which includes glucose φ^{FGu} and lactate φ^{FLc}. Thus, we consider the sets

$$\begin{aligned} &\mathcal{P}^{\alpha} := \{\mathrm{S},\,\mathrm{F}\} = \{\alpha_i \mid i = 1\ldots 2\} &&\text{for } \varphi^{\alpha} \mid \alpha \in \mathcal{P}^{\alpha},\\ &\mathcal{P}^{\mathrm{S}\beta} := \{\mathrm{Gy}\} = \{\beta_i \mid i = 1\} &&\text{for } \varphi^{\mathrm{S}\beta} \mid \beta \in \mathcal{P}^{\mathrm{S}\beta},\\ &\mathcal{P}^{\mathrm{F}\beta} := \{\mathrm{Gu},\,\mathrm{Lc}\} = \{\beta_i \mid i = 1\ldots 2\} &&\text{for } \varphi^{\mathrm{F}\beta} \mid \beta \in \mathcal{P}^{\mathrm{F}\beta}, \end{aligned} \tag{16}$$

so that with (1) the decomposition of mixture body is given via

$$\varphi = \varphi^{\mathrm{S}} + \varphi^{\mathrm{SGy}} + \varphi^{\mathrm{F}} + \varphi^{\mathrm{FGu}} + \varphi^{\mathrm{FLc}}. \tag{17}$$

We assume that glycogen is solely present in the tissue and glucose and lactate solely in the blood.

According to "Kinematics" section of Appendix, we define an independent motion function for the hepatocytes with $\boldsymbol{\chi}_{\mathrm{S}}(\mathbf{X}_{\mathrm{S}}, \mathrm{t})$, where $\mathbf{X}_{\mathrm{S}}$ defines the reference position of the hepatocytes and t denotes the time. Since glycogen φ^{SGy} is stored in the hepatocytes, we assume identical reference positions $\mathbf{X}_{\mathrm{SGy}} = \mathbf{X}_{\mathrm{S}}$. Moreover, the motion functions $\boldsymbol{\chi}_{\mathrm{S}}(\mathbf{X}_{\mathrm{S}}, \mathrm{t}) = \boldsymbol{\chi}_{\mathrm{SGy}}(\mathbf{X}_{\mathrm{S}}, \mathrm{t})$ and velocities $\mathbf{x}'_{\mathrm{SGy}} = \mathbf{x}'_{\mathrm{S}}$ are identical.

Due to convection and diffusion transport, see (67), the motions and velocities of blood, glucose and lactate have to be considered independently so that we define the independent reference positions $\mathbf{X}_{\mathrm{F}}$, $\mathbf{X}_{\mathrm{FGu}}$ and $\mathbf{X}_{\mathrm{FLc}}$, motion fields $\boldsymbol{\chi}_{\mathrm{F}}(\mathbf{X}_{\mathrm{F}}, \mathrm{t})$, $\boldsymbol{\chi}_{\mathrm{FGu}}(\mathbf{X}_{\mathrm{FGu}}, \mathrm{t})$ and $\boldsymbol{\chi}_{\mathrm{FLc}}(\mathbf{X}_{\mathrm{FLc}}, \mathrm{t})$ as well as velocities $\mathbf{x}'_{\mathrm{F}} = \mathbf{x}'_{\mathrm{F}}(\mathbf{X}_{\mathrm{F}}, \mathrm{t})$, $\mathbf{x}'_{\mathrm{FGu}} = \mathbf{x}'_{\mathrm{FGu}}(\mathbf{X}_{\mathrm{FGu}}, \mathrm{t})$ and $\mathbf{x}'_{\mathrm{FLc}} = \mathbf{x}'_{\mathrm{FLc}}(\mathbf{X}_{\mathrm{FLc}}, \mathrm{t})$.

In this approach, wave propagation and volume forces of the solutes are neglected. Thus, we exclude accelerations $\mathbf{x}''_{\boldsymbol{\alpha}} = \mathbf{o}$ and assume $\mathbf{b} = \mathbf{o}$, both for all phases.

We only assume an exchange of content between the solutes $\varphi^{\alpha\beta}$, which leads with $(15)_1$ to

$$\sum_{\boldsymbol{\alpha}=1}^{\kappa} \hat{\rho}^{\boldsymbol{\alpha}} = \hat{\rho}^{\mathrm{SGy}} + \hat{\rho}^{\mathrm{FGu}} + \hat{\rho}^{\mathrm{FLc}} = 0. \tag{18}$$

The moment production caused by the mass exchange of the solutes $\hat{\rho}^{\alpha\beta}\,\mathbf{x}'_{\beta}$, see $(14)_2$, is assumed to be significantly small and is neglected in the model. However, the interaction forces act between all components which result from $(15)_2$ in

$$\sum_{\boldsymbol{\alpha}=1}^{\kappa} \hat{\mathbf{p}}^{\boldsymbol{\alpha}} = \hat{\mathbf{p}}^{\mathrm{S}} + \hat{\mathbf{p}}^{\mathrm{F}} + \hat{\mathbf{p}}^{\mathrm{SGy}} + \hat{\mathbf{p}}^{\mathrm{FGu}} + \hat{\mathbf{p}}^{\mathrm{FLc}} = \mathbf{o}. \tag{19}$$

Moreover, we assume that the true density of the tissue matrix ρ^{SR} and the blood ρ^{FR} are constant ($(\rho^{\mathrm{SR}})'_{\mathrm{S}} = 0$, $(\rho^{\mathrm{FR}})'_{\mathrm{F}} = 0$), where the definition of the material time derivation is given in the "Kinematics" section of Appendix. The assumption of a material incompressible tissue is reasonable since the material compressibility of the tissue itself is much smaller than the compressibility of the overall empty porous body, see de Boer (2000), Ehlers (2002). Thus, the volumetric deformation of the mixture body results from the change of pore space, namely a change of the volume fraction n^{α} with $\alpha = \boldsymbol{\alpha}$, which leads to a macroscopic volumetric deformation. Since the volume fraction of the overall solutes $\varphi^{\alpha\beta}$ is negligible in contrast to the phases $\varphi^{\boldsymbol{\alpha}}$, see Sect. 2.2, we did not consider any volume change in dependency of a concentration variation and the saturation condition (8) reads

$$\mathrm{n}^{\mathrm{S}} + \mathrm{n}^{\mathrm{F}} = 1. \tag{20}$$

Finally, we consider the liver to be isothermal.

4 Field equations and constitutive modeling

In summary, a quasi-static, bi-phasic, ternary-substances model is derived taking into account an incompressible solid phase φ^{S} and an incompressible fluid phase φ^{F}, both carrying additional substances $\varphi^{\alpha\beta}$, under isothermal conditions with phase transition between the substances only. One internal substances $\varphi^{\mathrm{S}\beta}$ with $\mathrm{S}\beta \in \{\mathrm{Glycogen}\}$ stored in the solid phase and two external substances $\varphi^{\mathrm{F}\beta}$ with $\mathrm{F}\beta \in \{\mathrm{Glucose}, \mathrm{Lactate}\}$ that exist in the liquid phase are postulated, each indicated by the amount of concentration $\mathrm{c}^{\alpha\beta}$.

For the calculation of the unknown quantities, independent field equations are required. Therefore, we consider the constraint conditions associated with the mass exchange (18), the interaction forces (19), and the volume fractions (20). Provided that all phases are incompressible, the set of coupled field equations for the description of anisotropic perfusion and cell metabolism is given by the balance equations of mass for the solid and liquid phase,

$$(\mathrm{n}^{\mathrm{S}})'_{\mathrm{S}} + \mathrm{n}^{\mathrm{S}}\,\mathrm{div}\,\mathbf{x}'_{\mathrm{S}} = 0, \quad (\mathrm{n}^{\mathrm{F}})'_{\mathrm{F}} + \mathrm{n}^{\mathrm{F}}\,\mathrm{div}\,\mathbf{x}'_{\mathrm{F}} = 0, \tag{21}$$

see $(63)_{1,2}$, the balance equation of mass for the internal and external substances,

$$\begin{aligned} &(\mathrm{n}^{\mathrm{S}})'_{S}\,\mathrm{c}^{\mathrm{S}\beta} + \mathrm{n}^{\mathrm{S}}\,(\mathrm{c}^{\mathrm{S}\beta})'_{\mathrm{S}} + \mathrm{n}^{\mathrm{S}}\,\mathrm{c}^{\mathrm{S}\beta}\,\mathrm{div}\,\mathbf{x}'_{\mathrm{S}} - \hat{\mathrm{c}}^{\mathrm{S}\beta} = 0, \\ &(\mathrm{n}^{\mathrm{F}})'_{\mathrm{S}}\,\mathrm{c}^{\mathrm{F}\beta} + \mathrm{n}^{\mathrm{F}}\,(\mathrm{c}^{\mathrm{F}\beta})'_{\mathrm{S}} + \mathrm{div}\,\mathbf{j}^{\mathrm{F}\beta} + \mathrm{n}^{\mathrm{F}}\,\mathrm{c}^{\mathrm{F}\beta}\,\mathrm{div}\,\mathbf{x}'_{\mathrm{F}\beta} - \hat{\mathrm{c}}^{\mathrm{F}\beta} = 0, \end{aligned} \tag{22}$$

see (66), the balance equations of momentum for the constituents $\boldsymbol{\alpha}$,

$$\begin{aligned} \mathrm{div}\,\mathbf{T}^{\mathrm{S}} &= -\hat{\mathbf{p}}^{\mathrm{S}}\,, \quad \mathrm{div}\,\mathbf{T}^{\mathrm{F}} = -\hat{\mathbf{p}}^{\mathrm{F}}\,, \\ \mathrm{div}\,\mathbf{T}^{\mathrm{S}\beta} &= -\hat{\rho}^{\mathrm{S}\beta}\,\mathbf{x}'_{\mathrm{S}} - \hat{\mathbf{p}}^{\mathrm{S}\beta}\,, \\ \mathrm{div}\,\mathbf{T}^{\mathrm{F}\beta} &= \hat{\rho}^{\mathrm{F}\beta}(\mathbf{w}_{\mathrm{F}\beta\mathrm{S}} + \mathbf{x}'_{\mathrm{S}}) - \hat{\mathbf{p}}^{\mathrm{F}\beta}\,, \end{aligned} \tag{23}$$

considering the assumption that $\hat{\rho}^{\alpha} = 0$, see Sect. 3, and the material time derivative of the saturation condition,

$$-\,(\mathrm{n}^{\mathrm{S}})'_{\mathrm{S}} - (\mathrm{n}^{\mathrm{F}})'_{\mathrm{F}} + \mathrm{grad}\,\mathrm{n}^{\mathrm{F}} \cdot \mathbf{w}_{\mathrm{FS}} = 0\,, \tag{24}$$

see (49). The quantities $\mathbf{w}_{\mathrm{F}\beta\mathrm{S}} = \mathbf{x}'_{\mathrm{F}\beta} - \mathbf{x}'_{\mathrm{S}}$ in (23) and $\mathbf{w}_{\mathrm{FS}} = \mathbf{x}'_{\mathrm{F}} - \mathbf{x}'_{\mathrm{S}}$ in (24) are the velocities of the external solutes $\mathrm{c}^{\mathrm{F}\beta}$ and the liquid phase relative to the solid (seepage velocities). For the derivation of the balance equation of mass for the solutes (22), the relations stated in (12) and (13) have been used. Additionally, in $(22)_2$ the solvent flux $\mathbf{j}^{\mathrm{F}\beta} = \mathrm{n}^{\mathrm{F}}\mathrm{c}^{\mathrm{F}\beta}\mathbf{w}_{\mathrm{F}\beta\mathrm{S}}$, see (67), has been introduced.

4.1 Transversely isotropic permeability and remodeling

The permeability properties of a healthy liver are mainly influenced by the arrangement of the sinusoids, see Fig. 4. The sinusoids guide the blood along plates of hepatocytes from the portal triad to the central vein. This leads to an anisotropic permeability since the permeability parallel to the sinusoids is much higher than normal to the sinusoids.

In Debbaut et al. (2014), the influence of the transverse isotropic permeability and the vascular septum (vascular surfaces between adjacent lobules where part of the blood enters

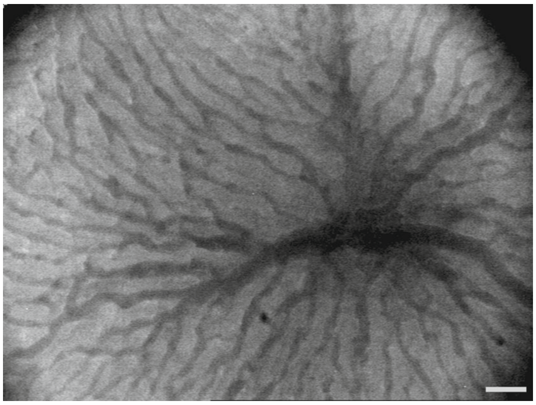

Fig. 4 Image of a liver lobule; the center shows the central vein surrounded by the sinusoids, Hall (2006). The hepatic microcirculation was observed with an optical device using the technique of Orthogonal Polarization Spectral (OPS) Imaging (Cytoscan, Cytometrics, Inc., Philadelphia, PA, USA). This device allows real-time microscopic observation of the microcirculation of organ surfaces in vivo. The probe is gently placed on a serous organ surface and emits polarized light with a wavelength of 550 nanometers. Light penetrates into the tissue where most of it depolarizes and creates a virtual light source in the tissue

the lobule) on the blood flow behavior in liver lobes have been investigated. It results that both the transverse isotropic permeability and the bordering vascular septum considerably change the pressure and velocity state. However, in human liver, the fibrovascular septum does not show distinct physicochemical and readily discernible morphologic properties.

Yet, the sinusoidal network is a highly adaptive system that also allows for focal distension of the sinusoidal diameter, resulting in a focally disparate sinusoidal flow. We could demonstrate that the dilatation of sinusoids allows for functional shunts in the case of hepatovenous outflow obstruction. Over time, these dilated sinusoidal structures undergo vascularization and transformation into sinusoidal canals—also showing CD34 expression of endothelial cells, cf. Dirsch et al. (2008). This finding highlights the plasticity of the sinusoidal meshwork and indicates that permanent changes in flow are accompanied by structural changes in the sinusoidal endothelial cells.

In Debbaut et al. (2014), the authors stated that in order to achieve homogenous sinusoidal perfusion vascular septa must be available—however, the direct morphologic proof is missing. The study of Teutsch (2005) could fill the gap. Surrounding portal tracts, he described an accentuation of perfusion indicating vascular septa. The author speculated that dilated sinusoids—termed septal sinusoids—could be the morphologic basis. However, these sinusoids are defined by their location in the watershed area of lobules but not based on histologic properties. Based on the pictures provided in Teutsch (2005), this area of vascular septa is not a continuous layer but shows gaps.

Since no signs of vascularization of sinusoids in the watershed areas containing septal sinusoids can be detected, it must be concluded that vascular septa are not structurally but may functionally be defined. Following this idea, sinusoids could act as functional vascular septa preferentially providing other sinusoids with blood. However, quite a lot of dynamics in respect to the extent of sinusoidal supply must be expected. In this study, we dispense with the assumption of a functional vascular septa and assume an inflow only at the portal triad. However, further studies will be done to investigate the influence of functional vascular septa on the inflow boundary conditions w.r.t liver lobules.

The transverse isotropic permeability is considered according to Ricken et al. (2010). In (24), we already introduced the seepage velocity $\mathbf{w}_{FS} = \mathbf{x}'_F - \mathbf{x}'_S$ as a material objective measure for the difference in velocity of the liquid and solid phase. The filter velocity $n^F\,\mathbf{w}_{FS}$ can be determined as

$$n^F\,\mathbf{w}_{FS} = (n^F)^2\,\mathbf{R}_F^{-1}\,(-\operatorname{grad}\lambda), \tag{25}$$

cf. Ricken et al. (2010), where $\mathbf{R}_F$ is a positive definite material parameter tensor representing the intrinsic hydraulic resistance of the lobule, λ is the pore pressure and $\mathbf{b}$ is the body force per unit mass. With this equation for the filtration velocity, the fact that the motions of both solid and liquid are connected by the interaction forces $\hat{\mathbf{p}}^L = -\hat{\mathbf{p}}^S$, and considering thermodynamic restrictions (see, e.g., Ricken and Bluhm (2009, 2010)), we propose the anisotropic intrinsic permeability of the liver tissue $\mathbf{K}_F$ as (cf. Pierce et al. 2013b)

$$\begin{aligned} \mathbf{K}_F &= (n^F)^2\,\mathbf{R}_F^{-1} = k_{0S}\left(\frac{n^F}{1-n^S_{0S}}\right)^m \mathbf{M}^*, \\ \mathbf{M}^* &= \kappa\,\mathbf{I} + \frac{1-3\kappa}{I_4}\,\mathbf{M}, \end{aligned} \tag{26}$$

where the (spatial) structural tensor $\mathbf{M}$ is defined as $\mathbf{M} = \mathbf{a}\otimes\mathbf{a} = \mathbf{F}_S\,\mathbf{a}_0\otimes\mathbf{F}_S\mathbf{a}_0 = \mathbf{F}_S\mathbf{M}_0\mathbf{F}_S^T$ and $I_4 = \mathbf{C}_S\cdot\mathbf{M}_0$. The permeability is deformation dependent, cf. Eipper (1998), and is parameterized by the initial Darcy permeability k_{0S} $[m^4/Ns]$ and m, which denotes dimensionless material parameter controlling the general isotropic deformation dependency of the permeability; also see, e.g., Ehlers (2002), Ricken (2002), Ricken and de Boer (2003). Inclusion of the volume fraction n^F relates to the change of permeability caused by the change of pore space, where n^S_{0S} denotes the reference solid volume fraction. Here, we use κ to define the range of permeabilities resulting from ideal alignment of sinusoids ($\kappa = 0$) to an isotropic distribution of the sinusoids ($\kappa = 1/3$).

In case of remodeling processes of sinusoids, i.e., the change of preferred direction of the mirco perfusion, an updating algorithm has been developed in Ricken et al. (2010) for 2D, which was enhanced for 3D in Werner et al. (2012). Therein, the evolution of preferred sinusoids direction is driven by the pressure gradient, see “Evolutionary approach for preferred flow direction” section of Appendix. We define remodeling as a change in structure that is achieved by reorganizing existing constituents, see Humphrey and Rajagopal (2002). A general study of biological remodeling is given in Garikipati et al. (2006) and specific applications can be found e.g. for bones in Hariton et al. (2007), the artery wall Kuhl and Holzapfel (2007); Valentin et al. (2013) or in glaucoma Grytz et al. (2012a, b).

5 Stresses and interaction forces

Postulating a Neo-Hookean Helmholtz free energy function for the solid

$$\psi^{\mathrm{S}} = \frac{1}{\rho^{\mathrm{S}}_{0\mathrm{S}}}\left\{\lambda^{\mathrm{S}}\,\frac{1}{2}\,(\ln \mathrm{J}_{\mathrm{S}})^2 - \mu^{\mathrm{S}}\ln \mathrm{J}_{\mathrm{S}} + \frac{1}{2}\,\mu^{\mathrm{S}}\,(\mathrm{tr}(\mathbf{C}_{\mathrm{S}}) - 3)\right\}, \tag{27}$$

with the Lamé constants λ^{S} and μ^{S} and the free energy function for the solutes

$$\psi^{\alpha\beta} = -\frac{1}{\mathrm{M}^{\beta}_{\mathrm{mol}}\,\mathrm{c}^{\alpha\beta}}\left\{\mathrm{R}\,\theta\left[\ln\left(\frac{\mathrm{c}^{\alpha\beta}}{\mathrm{c}^{\alpha\beta}_0}\right) + 1\right] + \mu^{\alpha\beta}_0\right\} \tag{28}$$

where R [J/(mol K)] is the general gas constant, θ [K] is the temperature of the mixture, $\mu^{\alpha\beta}_0$ [J/mol] is the reference chemical potential, and $\mathrm{c}^{\alpha\beta}_0[\mathrm{mol/m^3}]$ denotes the reference concentration.

The postulation of the Helmholtz free energy function in (28) is similar to that used in Ateshian (2007) and motivated by the fact that the resulting chemical potentials, cf. $(29)_4$, correspond to the formulation given in literature, see eg. Job and Herrmann (2006). Inserting (27) and (28) into the restrictions resulting from the evaluation of entropy inequality (58) we obtain

$$\begin{aligned}
\mathbf{T}^{\mathrm{S}} &= \frac{1}{\mathrm{J}_{\mathrm{S}}}(\lambda^{\mathrm{S}}\ln\mathrm{J}_{\mathrm{S}}\,\mathbf{I} + 2\mu^{\mathrm{S}}\mathbf{K}_{\mathrm{S}}) - \mathrm{n}^{\mathrm{S}}\,\lambda\,\mathbf{I}\\
&= \mathbf{T}^{\mathrm{S}}_{\mathrm{E}} - \mathrm{n}^{\mathrm{S}}\,\lambda\,\mathbf{I},\\
\mathbf{T}^{\mathrm{F}} &= \mathrm{n}^{\mathrm{F}}\left(\mathrm{R}\theta\ln\left(\frac{\mathrm{c}^{\mathrm{F}\beta}}{\mathrm{c}^{\mathrm{F}\beta}_0}\right) + \mu^{\mathrm{F}\beta}_0\right)\mathbf{I} - \lambda\,\mathrm{n}^{\mathrm{F}}\,\mathbf{I}\\
&= \mathrm{n}^{\mathrm{F}}\,(\mu^{\mathrm{F}\beta} - \lambda)\,\mathbf{I} = -\mathrm{n}^{\mathrm{F}}\,\mathrm{p}^{\mathrm{FR}}\,\mathbf{I},\\
\mathbf{T}^{\mathrm{F}\beta} &= -\mathrm{n}^{\mathrm{F}}\left(\mathrm{R}\theta\ln\left(\frac{\mathrm{c}^{\mathrm{F}\beta}}{\mathrm{c}^{\mathrm{F}\beta}_0}\right) + \mu^{\mathrm{F}\beta}_0\right)\mathbf{I}\\
&= -\mathrm{n}^{\mathrm{F}}\,\mu^{\mathrm{F}\beta}\,\mathbf{I},\\
\mu^{\alpha\beta} &= \mathrm{R}\,\theta\,\ln\frac{\mathrm{c}^{\alpha\beta}}{\mathrm{c}^{\alpha\beta}_0} + \mu^{\alpha\beta}_0,
\end{aligned} \tag{29}$$

where use has been made of the Karni-Reiner strain tensor $\mathbf{K}_{\mathrm{S}} = 1/2\,(\mathbf{B}_{\mathrm{S}} - \mathbf{I})$, the left Cauchy-Green tensor $\mathbf{B}_{\mathrm{S}} = \mathbf{F}_{\mathrm{S}}\,\mathbf{F}^{\mathrm{T}}_{\mathrm{S}}$, the extra stress $\mathbf{T}^{\mathrm{S}}_{\mathrm{E}}$ of the solid phase, the fluid pressure $\mathrm{p}^{\mathrm{FR}} = \lambda - \lambda^{\mathrm{F}\beta}$ and the chemical potential $\mu^{\alpha\beta}$ of the solutes according to $(58)_3$, cf. e.g. Job and Herrmann (2006); Ateshian (2007).

The assumption of an isotropic solid stress-strain behavior is a simplification. However, this simplification seems to be reasonable since liver lobule tissue (in contrast to the collagenous liver capsule, cf. Kerdok (2006)) includes no collagen fibers and the stiffness behavior results from the venous pressure, cf. Millonig et al. (2010). However, a minor anisotropic solid tissue response can be expected from the inner liver lobule structure, since the sinusoids are oriented transversal isotropically. If the resulting (locally) transversely isotropic stress behavior should also be reflected in the constitutive model, an additive decomposition of the superimposed solid Helmholtz free energy function ψ^{S} is suggested into an isotropic matrix part $\psi^{\mathrm{S}}_{\mathrm{IM}}$, and a transversely isotropic part $\psi^{\mathrm{S}}_{\mathrm{FF}}$, i.e.,

$$\psi^{\mathrm{S}} = \psi^{\mathrm{S}}_{\mathrm{IM}}(\mathrm{J}_{\mathrm{S}},\ I_1) + \psi^{\mathrm{S}}_{\mathrm{FF}}(I_1,\ I_4), \tag{30}$$

where $\mathrm{J}_{\mathrm{S}} = \det\mathbf{F}_{\mathrm{S}}$ (the Jacobian), $\mathrm{I}_1 = \mathrm{tr}\mathbf{C}_{\mathrm{S}}$, $I_4 = \mathbf{C}_{\mathrm{S}} \cdot \mathbf{M}_0$, with $\mathbf{M}_0 = \mathbf{a}_0 \otimes \mathbf{a}_0$ as (Lagrangian) structural tensor. A detailed exhibition of this representation is given in Pierce et al. (2013a).

6 Incorporation of the cell metabolism

As a proof of principle for the integration of cellular metabolism into a tissue-level model of blood perfusion and substrate supply, we combined a reduced model of hepatic glucose metabolism with the 3D-FEM model for anisotropic perfusion.

6.1 Reduced metabolic model

The reduced metabolic model was derived from a detailed kinetic model of hepatic glucose metabolism König et al. (2012). It fully replicates the quasi-stationary behavior of the detailed model, i.e., uptake or release rate of glucose depending on the blood glucose concentration (see Fig. 5). The reduced model comprises as variables the three central metabolites of hepatic glucose metabolism: blood glucose (φ^{FGu}), blood lactate (φ^{FLc}) and hepatic glycogen (φ^{SGy}). The levels of these metabolites are governed by effective reactions: $\mathrm{v_{HGU}}$ (hepatic glucose utilization/ hepatic glucose production), $\mathrm{v_{GS}}$ (glycogen synthesis/ glycogenolysis) and $\mathrm{v_{GLY}}$ (glycolysis/ gluconeogenesis). The kinetics of the effective reactions are described by polynomial regression functions of third order $\mathrm{p}(\varphi^{\mathrm{FGu}}, \varphi^{\mathrm{SGy}}, \varphi^{\mathrm{FLc}})$ which were fitted to the steady-state response of the detailed kinetic model (Fig. 6, see Sect. 4 for polynomial coefficients).

$$\begin{aligned}
\mathrm{v_{HGU}}(\varphi^{\mathrm{FGu}}, \varphi^{\mathrm{SGy}}, \varphi^{\mathrm{FLc}}) &= \mathrm{p_{HGU}}(\varphi^{\mathrm{FGu}}, \varphi^{\mathrm{SGy}}, \varphi^{\mathrm{FLc}})\\
\mathrm{v_{GLY}}(\varphi^{\mathrm{FGu}}, \varphi^{\mathrm{SGy}}, \varphi^{\mathrm{FLc}}) &= \mathrm{p_{GLY}}(\varphi^{\mathrm{FGu}}, \varphi^{\mathrm{SGy}}, \varphi^{\mathrm{FLc}})\\
\mathrm{v_{GS}}(\varphi^{\mathrm{FGu}}, \varphi^{\mathrm{SGy}}, \varphi^{\mathrm{FLc}}) &= \mathrm{v_{HGU}}(\varphi^{\mathrm{FGu}}, \varphi^{\mathrm{SGy}}, \varphi^{\mathrm{FLc}})\\
&\quad - \mathrm{v_{GLY}}(\varphi^{\mathrm{FGu}}, \varphi^{\mathrm{SGy}}, \varphi^{\mathrm{FLc}})
\end{aligned} \tag{31}$$

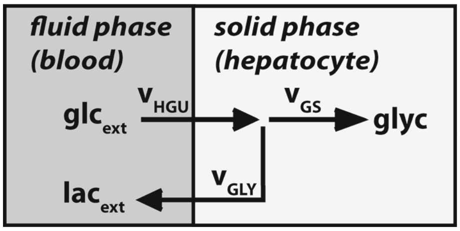

Fig. 5 The reduced model of hepatic glucose metabolism comprises the variables glucose (φ^{FGu}) and lactate (φ^{FLc}) in the fluid phase (blood) and glycogen (φ^{SGy}) in the solid phase (hepatocyte). The effective reactions $\mathrm{v}_{\mathrm{HGU}}$, $\mathrm{v}_{\mathrm{GLY}}$ and v_{GS} are modeled by polynomial regression functions which were fitted to a large set of the steady-state responses of the detailed kinetic model König et al. (2012) with $\mathrm{v}_{\mathrm{HGU}} < 0$ hepatic glucose production, $\mathrm{v}_{\mathrm{HGU}} > 0$ hepatic glucose utilization, $\mathrm{v}_{\mathrm{GLY}} < 0$, gluconeogenesis, $\mathrm{v}_{\mathrm{GLY}} > 0$ glycolysis, $\mathrm{v}_{\mathrm{GS}} < 0$ glycogenolysis, $\mathrm{v}_{\mathrm{GLY}} > 0$ glycogen synthesis

The resulting ordinary differential equations describing the changes in glucose, glycogen and lactate (one molecule of glucose is converted to two molecules of lactate in glycolysis) are

$$\begin{aligned} -\mathrm{v}_{\mathrm{HGU}}(\varphi^{\mathrm{FGu}}, \varphi^{\mathrm{SGy}}, \varphi^{\mathrm{FLc}}) &= \widetilde{\hat{c}^{\mathrm{FGu}}},\\ \mathrm{v}_{\mathrm{GS}}(\varphi^{\mathrm{FGu}}, \varphi^{\mathrm{SGy}}, \varphi^{\mathrm{FLc}}) &= \widetilde{\hat{c}^{\mathrm{SGy}}},\\ 2 \cdot \mathrm{v}_{\mathrm{GLY}}(\varphi^{\mathrm{FGu}}, \varphi^{\mathrm{SGy}}, \varphi^{\mathrm{FLc}}) &= \widetilde{\hat{c}^{\mathrm{FLc}}}, \end{aligned} \tag{32}$$

where $\widetilde{\hat{c}^{\alpha\beta}}$ denotes the concentration exchange rate on the cell level. The polynomial fit of the steady-state responses is possible because the detailed kinetic model reaches quasi-steady state within minutes, much faster than the simulated timescales of the 3D-FEM model. Interestingly, the reduced model is able to reproduce the main model features and behavior of the full model in the physiological range, like the ability to switch between hepatic glucose production (HGP) and hepatic glucose utilization (HGU), beween glycolysis and gluconeogenesis and between glycogen storage and glycogenolysis depending on the external conditions and the internal state (hepatic glycogen) (Fig. 6).

Owing to the model reduction approach, the mathematical complexity of the integrated model and hence the simulation runtime for the ordinary differential equation system of the metabolic sub-module could be significantly reduced. The reduction in the glucose model from 47 species and 49 reactions to 3 species and 3 reactions resulted in a runtime reduction of a factor 10–20 for simulations with the single cell model, namely stationary simulations and the simulations of the daily glucose profiles.

6.2 Coupling of micro- and cell level

For the homogenization from the cell to the microlevel, we use the concept of representative volume elements (RVE) and assume further that the length scale L_{cell} of the cellular level is much smaller in contrast to the length scale L_{micro} of the lobule level ($L_{\mathrm{cell}} \ll L_{\mathrm{micro}}$). Arbitrary scalar quantities on the lobule level $\{\cdot\}$ are then represented by the homogenization

$$\{\cdot\} = \frac{1}{\mathrm{V}} \int_{\partial \mathrm{B}_{\mathrm{S}}} \widetilde{\{\cdot\}}\ \mathrm{dv}, \tag{33}$$

relating to the volume $V = |\mathrm{B}_{\mathrm{S}}|$ of the RVE where $\widetilde{\{\cdot\}}$ denotes arbitrary scalar quantities on the cell level. The microscopic quantities of the concentration exchange rates are then given with

$$\begin{aligned} \hat{c}^{\mathrm{FGu}} &= \frac{1}{\mathrm{V}} \int_{\partial \mathrm{B}_{\mathrm{S}}} \{\widetilde{\hat{c}^{\mathrm{FGu}}}\}\ \mathrm{dv},\\ \hat{c}^{\mathrm{FLc}} &= \frac{1}{\mathrm{V}} \int_{\partial \mathrm{B}_{\mathrm{S}}} \{\widetilde{\hat{c}^{\mathrm{FLc}}}\}\ \mathrm{dv},\\ \hat{c}^{\mathrm{SGy}} &= \frac{1}{\mathrm{V}} \int_{\partial \mathrm{B}_{\mathrm{S}}} \{\widetilde{\hat{c}^{\mathrm{SGy}}}\}\ \mathrm{dv}. \end{aligned} \tag{34}$$

The algorithm for the metabolic model itself has been imbedded into the FE-model via a staggered algorithm. The system of ordinary differential equations is solved with dependency of actual quantities in each Gauss point calculating the rate of concentration exchange for each solute $\hat{c}^{\alpha\beta}$.

7 Numerical treatment of macro scale

Weak formulations are formed within the framework of a standard Galerkin procedure. Under consideration of all assumptions, the constrain conditions and the constitutive equations, we obtain the set $\Re$ of unknown quantities with six independent fields $\Re = \Re(\mathbf{x}, \mathrm{t}) = \{\mathbf{u}_{\mathrm{S}}, \mathbf{w}_{\mathrm{FS}}, \mu^{\alpha\beta}, \mathrm{p}^{\mathrm{FR}}\}$ wherein $\mathbf{u}_{\mathrm{S}}$ denotes the displacement of the solid and $\mu^{\alpha\beta}$ represents the chemical potential. We account for μ^{SGy} (glycogen solely in the tissue), μ^{FGu} (glucose solely in the blood), and μ^{FLc} (lactate solely in the blood). The filter velocity $\mathrm{n}^{\mathrm{F}}\,\mathbf{w}_{\mathrm{FS}}$ is calculated using the balance of momentum from (25). Finally, the set of unknown quantities $\Re$ can be reduced to five quantities with

$$\Re = \Re(\mathbf{x}, \mathrm{t}) = \{\mathbf{u}_{\mathrm{S}}, \mu^{\alpha\beta}, \mathrm{p}^{\mathrm{FR}}\}\,. \tag{35}$$

In order to determine the independent fields given in (35), weak forms have to be formulated. Therefore, for the mixture, we use the sum of the balance equations of momentum $(23)_1$ multiplied with the weight function $\delta\mathbf{u}_{\mathrm{S}}$ as well as the balance equations of mass $(21)_{1,2,3}$ for the mixture, internal and external solutes multiplied with the weight functions $\delta\mathrm{p}^{\mathrm{FR}}$, $\delta\mu^{\mathrm{SGy}}$, and $\delta\mu^{\mathrm{F}\beta}$ with $\beta \in \{\mathrm{Gu}, \mathrm{Lc}\}$, respectively. As a result, the used set of equations according to the actual placement can be evaluated to weak forms.

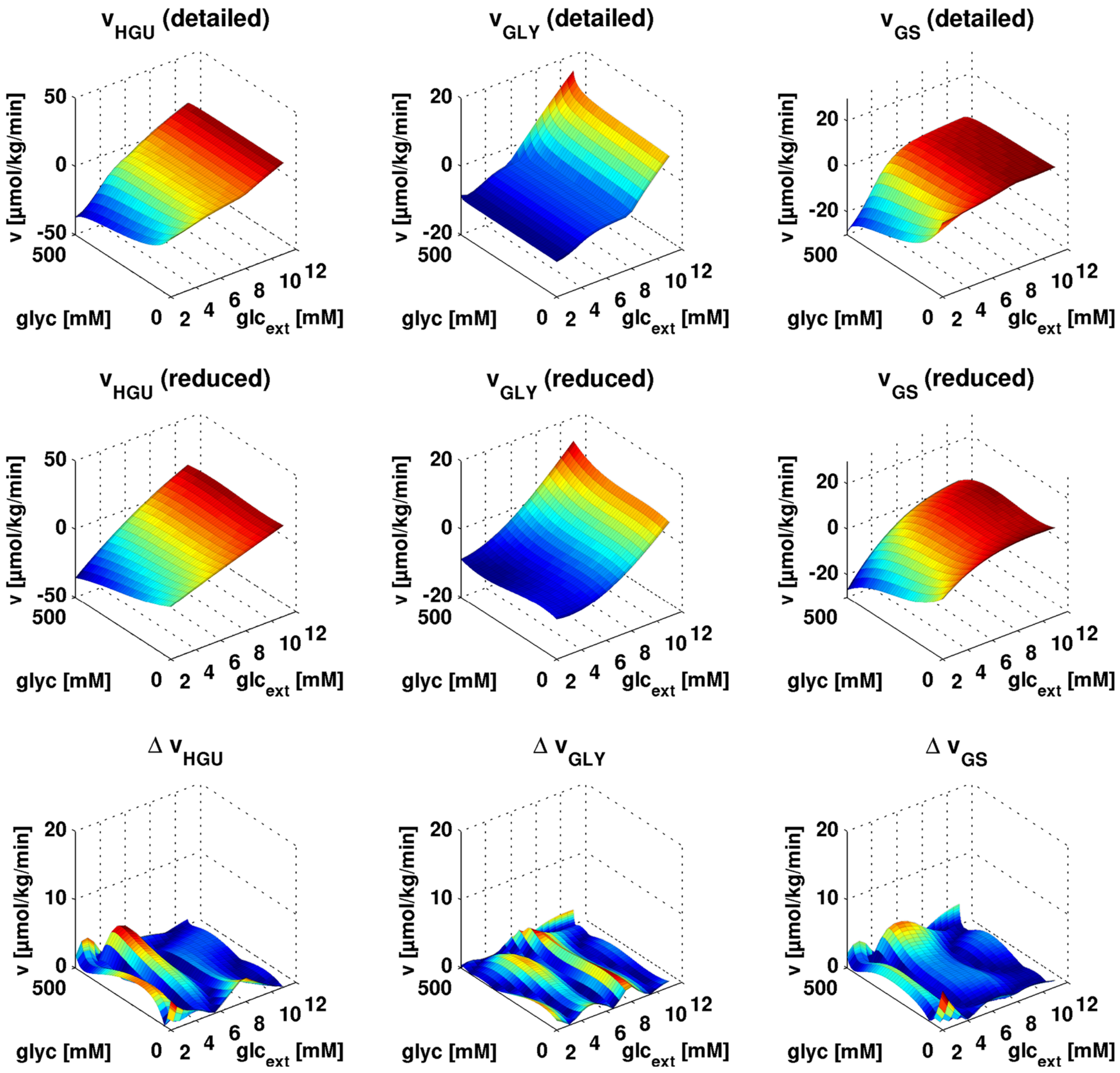

Fig. 6 Evaluation of the reduced metabolic sub-model. HGP/HGU (v_{HGU}), gluconeogenesis/glycogenolysis (v_{GLY}) and glycogenolysis/glycogen synthesis (v_{GS}) depending on blood glucose ($\varphi^{FGu} = glc_{ext}$) and glycogen ($\varphi^{SGy} = glyc$) for the detailed kinetic model (*top row*), the reduced model via polynomial fitting (*middle row*) and the absolute difference between detailed model and reduced model (*third row*). The reduced model is able to describe the behavior of the full kinetic model for a wide range of different model inputs

- B. o. Momentum for the Mixture

$$\int_{B_S} \left\{ \Big(\sum_{\alpha}^{S,\,F,\,\alpha\beta} \mathbf{T}^{\alpha} \Big) \cdot \operatorname{grad} \delta \mathbf{u}_S \right\} \mathrm{dv} - \int_{B_S} \{ \hat{\rho}^{F\beta}\, \mathbf{w}_{F\beta S} \cdot \delta \mathbf{u}_S \} \,\mathrm{dv} = \int_{\partial B_S} \{ \mathbf{t} \cdot \delta \mathbf{u}_S \} \,\mathrm{da} \qquad (36)$$

- B. o. Mass for the Mixture

$$\int_{B_S} \left\{ n^F \mathbf{w}_{FS} \cdot \operatorname{grad} \delta p^{FR} \right\} \mathrm{dv} + \int_{B_S} \left\{ \mathrm{tr} \mathbf{D}_S \, \delta p^{FR} \right\} \mathrm{dv} = \int_{\partial B_S} \left\{ n^F \mathbf{w}_{FS} \cdot \mathbf{n} \right\} \delta p^{FR} \,\mathrm{da} \quad (37)$$

- B. o. Mass for Internal Solute

$$\int_{B_S} \left\{ (n^S\, c^{SGy})'_S \; \delta \mu^{SGy} \right\} \mathrm{dv} + \int_{B_S} \left\{ c^{SGy}\, n^S\, \mathrm{tr} \mathbf{D}_S - \hat{\rho}^{SGy}_{mol} \right\} \delta \mu^{SGy} \,\mathrm{dv} = 0 \qquad (38)$$

- B. o. Mass for External Solutes with $\beta \in \{\mathrm{Gu},\ \mathrm{Lc}\}$

$$
\begin{aligned}
&\int_{\mathrm{B_S}} \left\{ (\mathrm{n^F\, c^{F\beta}})'_{\mathrm{S}}\ \delta\mu^{\mathrm{F}\beta} \right\} \mathrm{dv} - \int_{\mathrm{B_S}} \left\{ \mathbf{j}^{\mathrm{F}\beta} \cdot \mathrm{grad}\, \delta\mu^{\mathrm{F}\beta} \right\} \mathrm{dv} \\
&\quad + \int_{\mathrm{B_S}} \left\{ \mathrm{c^{F\beta}\, n^F\, tr}\mathbf{D}_{\mathrm{S}} - \hat{\rho}^{\mathrm{F}\beta}_{\mathrm{mol}} \right\} \delta\mu^{\mathrm{F}\beta}\, \mathrm{dv} \\
&\quad = \int_{\partial\mathrm{B_S}} \left\{ \mathbf{j}^{\mathrm{F}\beta}\, \delta\mu^{\mathrm{F}\beta} \cdot \mathbf{n} \right\} \mathrm{da}
\end{aligned}
\tag{39}
$$

The weak forms of the balance equations are implemented in the finite element program FEAP developed by Taylor, UC Berkeley . The finite element discretization was realized with the Galerkin method. In order to ensure stable numerical results, the so-called Taylor-Hood elements are used with quadratic ansatz functions for $\mathbf{u}_{\mathrm{S}}$ and linear ansatz functions for $\mathrm{p^{FR}}$ and $\mu^{\alpha\beta}$.

8 Numerical example: coupled perfusion and metabolism

8.1 Setup and material parameters

Spatially heterogenous glycogen storage within the lobule is a well-known phenomenon in hepatic glucose metabolism, cf. Corrin and Aterman (1968) or Sasse (1975). In the presented numerical example, we performed a simulation on the lobule geometry analog to the experiments performed by Babcock and Cardell (1974), namely the analysis of glycogen storage patterns in the liver under controlled feeding cycles (Fig. 7). In the beginning of the 24-h feeding cycle, rats were fed for the first 2 h, then fasted for the remaining 22 h. For the simulation, glucose profiles corresponding to 2 h of food intake and 22 h of fasting based on 24-h profiles of plasma glucose (cf. Stanhope et al. 2008; Yuen et al. 2012) were used as periportal input profiles for the model (Fig. 8).

The geometry of the applied finite element model and arrangement of boundary conditions are shown in Fig. 9. Due to axis symmetry and convenient handling of mirroring (which is a time-consuming and semi-automatic post-processing step) the results for a full lobule representation, one-quarter of the hexagonal-shaped lobule has been considered with respective symmetric boundary conditions along the two-symmetry axis.

The dimensions of the lobule are based on reported values for the diameter of human hepatic lobules of 1.0–1.3 mm, cf. Kuntz and Kuntz (2006), and in line with the distance between central veins of ∼1 mm, cf. Lautt (2009). These values are comparable to the lobules diameter in rats of 809±199 μm (SD, $n = 79$, young rat, SEM of corrosion cast), cf. Warren et al. (2008). Due to variation in reported values for diameters of the central vein and periportal triad, representative values have been chosen, cf. Maass-Moreno and Rothe (1997), Teutsch et al. (1999), Teutsch (2005), Burt et al. (2007).

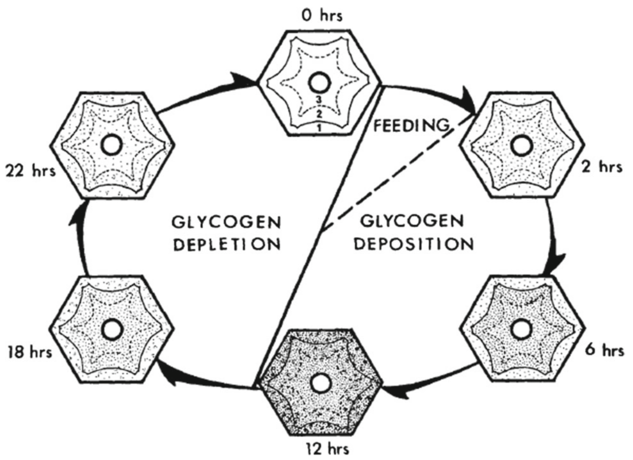

Fig. 7 Schematic sketch of the feeding cycle showing duration and typical patterns for glycogen in a single lobule during deposition and depletion. After feeding (0–2 h), glycogen is deposited, whereas in the fasting phase, glycogen is depleted. Figure reproduced from Babcock and Cardell (1974)

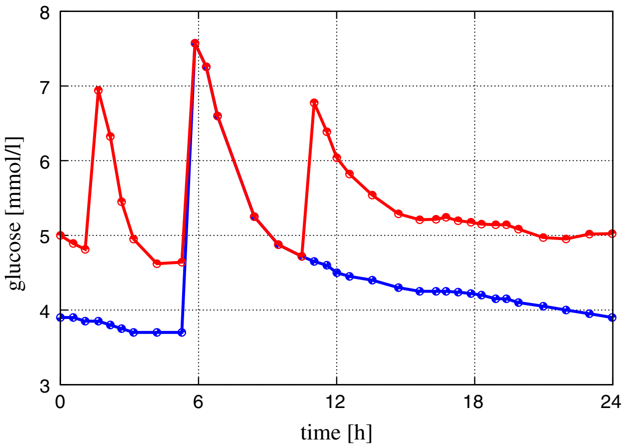

Fig. 8 Glucose profile corresponding to 2 h of food intake and 22 h of fasting based on 24-h profiles of plasma glucose (*blue*) and for a 3-meal 24-feeding schedule (*red*). Experimental data from (Stanhope et al. 2008; Yuen et al. 2012)

In case of elastic properties, values for Poisson's ratio are reported between 0.35 and 0.4, while values for Young's modulus vary substantially. Values range from 2.5 kPa up to 100 kPa, cf. Schwartz et al. (2005), Nava et al. (2008), Evans et al. (2013), Brown et al. (2003), Samur et al. (2005). Due to lack of precise parameter estimation and for convenience, we applied a Young's modulus of 28 kPa and a Poisson's ratio of 0.4.

The volume fractions of liver tissue were reported as 78 % for parenchymal cells, i.e., hepatocytes, sinusoidal blood vol-

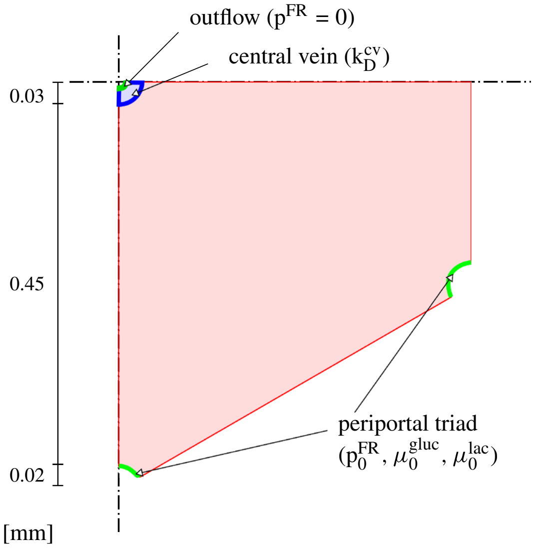

Fig. 9 Depiction of the applied geometry and boundary conditions

ume of 11 % and extravascular volumes of ∼5 % in morphological studies in rats, cf. Blouin et al. (1977) or Lautt (2009). This is in line with data from isolated perfused human liver reporting sinusoidal blood volume fraction as 9–15 % and extravascular fluid volume as 5–8% (14–22% fluid fraction), cf. Villeneuve et al. (1996). The volume fractions were set as 75 % (hepatocytes, solid) and 25 % (sinusoidal and extravascular fluid), respectively.

The permeability Darcy parameter has been fitted to recorded blood velocities from literature. In animal, experiments measured blood velocities in sinusoids range from 0–400 μm/s with mean values of 69 μm/s in mouse and 180 μm/s in rat, cf. MacPhee et al. (1995). We take an estimated but physiological pressure difference of 1 mmHg (133 Pa) from periportal triad to the outflow into account, cf. Maass-Moreno and Rothe (1997), see Fig. 10a. A resulting mean blood velocity of 152 μm/s has been calculated, see Fig. 10b.

1. Constant pressure at the periportal triad and central vein
2. Time-depending Dirichlet boundary condition for glucose at the periportal triad
3. Constant Dirichlet boundary condition for lactate at the periportal triad

The central vein has been implemented as a region with increased permeability and a small outflow at its center. Therefore, the solutes in the liquid phase get drained out of the lobule without adding additional boundary conditions for the solutes at the central vein. Material parameters and boundary values are summarized in Table 1.

Regarding the anisotropic permeability, we started with the unphysiological assumption that the direction of all sinusoids is parallel. As time goes on, the sinusoids orient in the direction of the pressure gradient. Finally, the sinusoids are oriented parallel to the pressure gradient and no further reorientation occurs, see Fig. 10. This stationary solution can be defined as the optimal state and is used as a reasonable physiological starting configuration for the presented numerical examples.

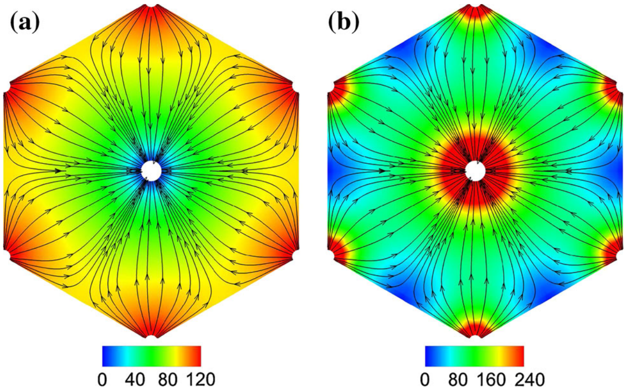

Fig. 10 Contour plot for the pressure and velocity destribution. 1 mmHg (133 Pa) is the applied, estimated pressure difference between the periportal triad and the outflow (resulting pressure gradient between periportal triad and central vein is ∼ 0.9 mmHg $\hat{=}$ 120 Pa). Maximum velocity is about 500 μm/s, average velocity in the lobule is 152 μm/s. Due to constant boundary conditions for the pressure applied to all simulations, pressure and velocity distributions remain constant over time for every shown simulation. Stream lines denote the preferred flow direction for the stationary solution using anisotropic permeability. **a** Distribution for pore pressure p^{FR} (N/m^2), **b** Distribution for fluid velocity $\mathbf{w}_{LS}$ (μm/s)

Table 1 Material parameters of liver lobule

Param.	Value	Unit	Remark
n_{0S}^S	0.75	–	Volume fraction solid
n_{0S}^F	0.25	–	Volume fraction fluid
μ^S	$1 \cdot 10^4$	Pa	Lamé constant
λ^S	$4 \cdot 10^4$	Pa	Lamé constant
R_0	8.3144	J/molK	Gas constant
T_0	280	K	Temperature
k_D^F	$6 \cdot 10^{-10}$	m/s	Darcy permeability
$k_D^{F,cv}$	$6 \cdot 10^{-5}$	m/s	Darcy permeability at central vein
$\mathbf{a}_0$	$\begin{pmatrix}-1/\sqrt{2}\\ 1/\sqrt{2}\\ 0\end{pmatrix}$	–	Initial flow direction
κ	0.2	–	Degree of anisotropy
δ_t	0.1	–	Virtual damping param

8.2 Results

Daily variation of glucose metabolism in the lobules was simulated under typical glucose profiles (Fig. 8). To analyze the local differences in glucose metabolism, the time courses of

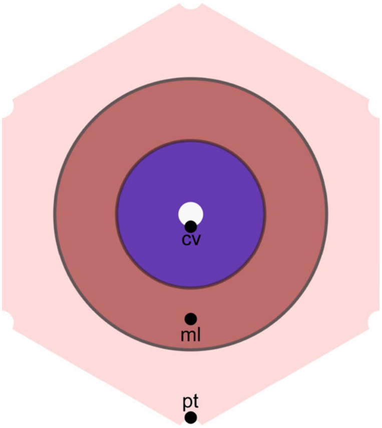

Fig. 11 Depiction of the centrilobular, midlobular and periportal points picked for evaluation. Storage of glucose, glycogen and lactate within the colored zones is evaluated in Fig. 12 for one-meal cycle and Fig. 14 for three-meal cycle

glucose, lactate and glycogen and the corresponding fluxes of glucose utilization/production (HGU/HGP), glycogen synthesis/glycogenolysis and gluconeogenesis/glycolysis (Fig. 12) were evaluated at various positions within the lobule (Fig. 11), namely periportal (pt), midlobular (ml) and centrilobular (cv). Differences from periportal to centrilobular in glucose, glycogen and lactate are observed. Glycogen is lower periportal, whereas lactate is higher in the periportal region. The glycogen decreasing at periportal corresponds qualitatively to experimental observations, cf. Saitoh et al. (2010). However, more effort will be done to validate the profiles experimentally in future studies.

Depending on the nutritional state, glucose is either lower periportal during fasting, due to glucose production within the lobules, or becomes higher periportal then centrilobular after food uptake, a consequence of the glucose storage as glycogen within the lobule which decreases the intra-lobular glucose concentration towards the centrilobular region. The dual role of the liver as either glucose producer between meals (HGP) or glucose consumer after meals (HGU) is affirmed by the numerical results given in Fig. 13. Moreover, the important role of glycogen as glucose buffer can be observed throughout the lobule (Fig. 13). In between meals, glycogen is converted to glucose via glycogenolysis and subsequently exported into the blood, whereas after food uptake accompanied with rising glucose levels, glucose is taken up by the hepatocytes and stored via glycogen synthesis. Depending on the rate of glycolysis, which converts glucose to lactate, varying amounts of lactate are produced. Qualitative similar behavior to the one-meal cycle can be observed in the multiple meal regime (Figs. 14, 15) with a switch of hepatic glucose metabolism between glucose production and consumption as well as between glycogen storage and glycogenolysis depending on the blood glucose concentrations. Due to the coupling of the glucose metabolism in the solid phase via the transport of glucose and lactate in the fluid phase, spatial patterns of glucose, glycogen and lactate arise within the lobules under typical nutritional regimes (Figs. 16, 17, 18).

9 Discussion

The model simulations show the important metabolic role of the liver lobules as ’glucostat,’ taking up glucose under high blood glucose concentrations as occurs postprandial via hepatic glucose utilization (HGU) and switching to hepatic glucose production (HGP) when blood glucose values fall between meals. Glycogen synthesis as well as glycolysis contribute to HGU, whereas the glucose in HGP consists of de novo synthesized glucose in gluconeogenesis and glucose from glycogen. The important role of glycogen as glucose buffer is underlined, with glycogen storage under hyperglycemic conditions and glycogenolysis when blood glucose values fall (König et al. 2012; Nuttal et al. 2008; Radziuk and Pye 2001; Wahren and Ekberg 2007).

9.1 Heterogeneity in liver metabolism and hepatic glycogen patterns

Very interestingly, metabolic gradients along the sinusoid in glucose and lactate are established due to the role of glucose and lactate as either substrate or product depending on the actual glucose concentrations. The resulting ratios of periportal to perivenous differences in glucose are in line with reported values for most carbon substrates like glucose and lactate in the range from 10 to 50 % (Jungermann 1986). Even without a zonated model of hepatic metabolism, i.e., zonated metabolic capacities in the pathways, zonation in metabolism arises as a consequence of substrate and product gradients within the tissue model. Due to the architecture of the liver, heterogeneity in the local response arises as an emergent system property. Consequently, glycogen is synthesized and degraded heterogenously and thereby also distributed heterogenously over the parenchyma during filling or emptying of the glycogen stores, a well-known effect in liver glycogen metabolism (Corrin and Aterman 1968; Sasse 1975). As an emerging model behavior, the spatially heterogenous storage and utilization of glycogen results in hepatic glycogen patterns within the lobule (Babcock and Cardell 1974).

9.2 Multiscale model and model reduction

Via the simultaneous evaluation of the multiple scales, namely lobule and cellular scale, the presented multiscale model of hepatic metabolism integrated with perfusion provided access to emerging system behavior, that would not have been observable using single scale techniques. This is

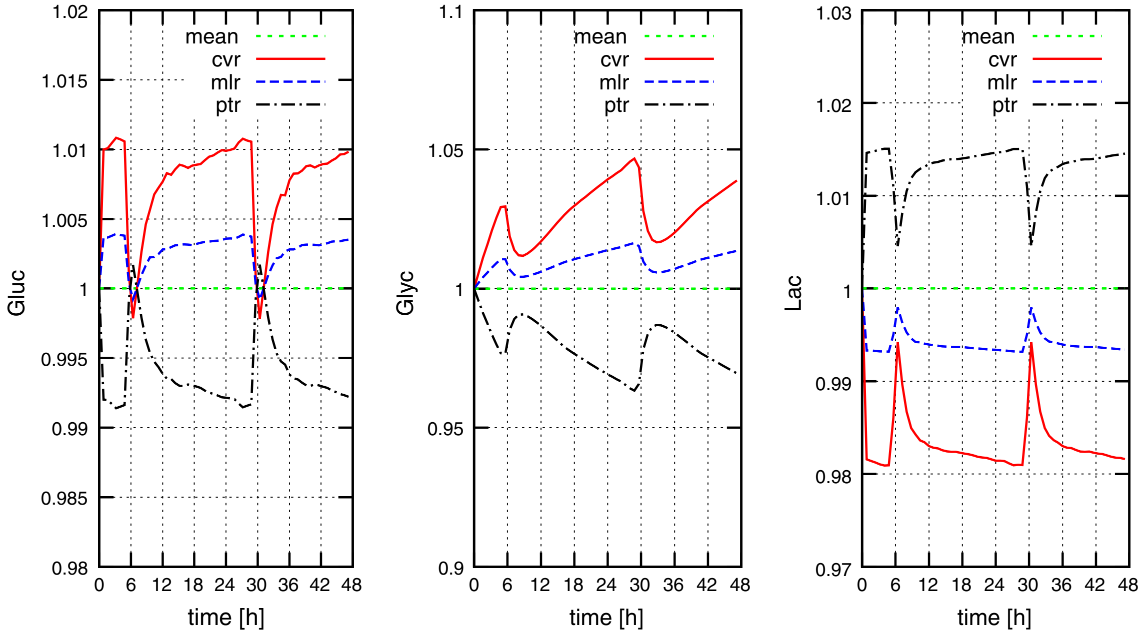

Fig. 12 Evaluation of glucose, glycogen and lactate in the centrilobular region (CVR), midlobular region (MLR) and periportal region(PTR) for a one-meal cycle compared with the mean value of the respective concentration in the whole lobule

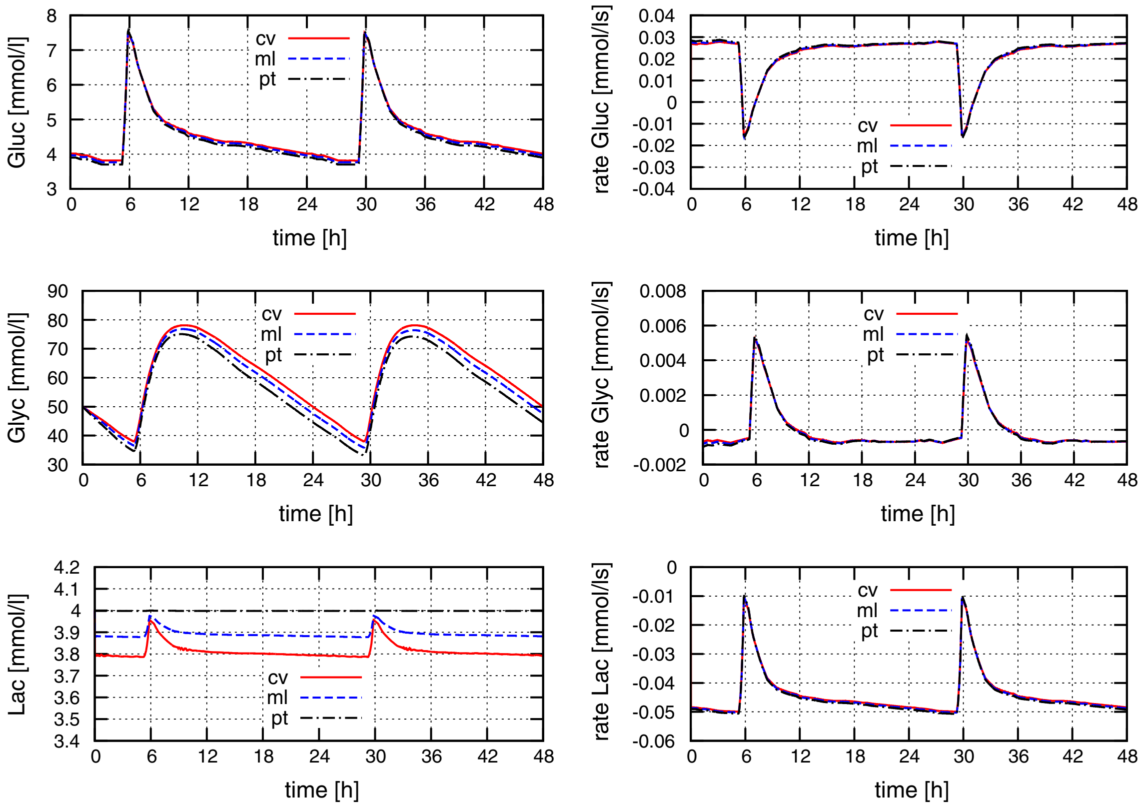

Fig. 13 Evaluation of glucose, glycose and lactate at three single points along the shortest path between the periportal triad and the central vein for the case of a single meal cycle. One point is located at the central vein (CV), the second is located midlobular (ML) and the third at the portal triad (PT)

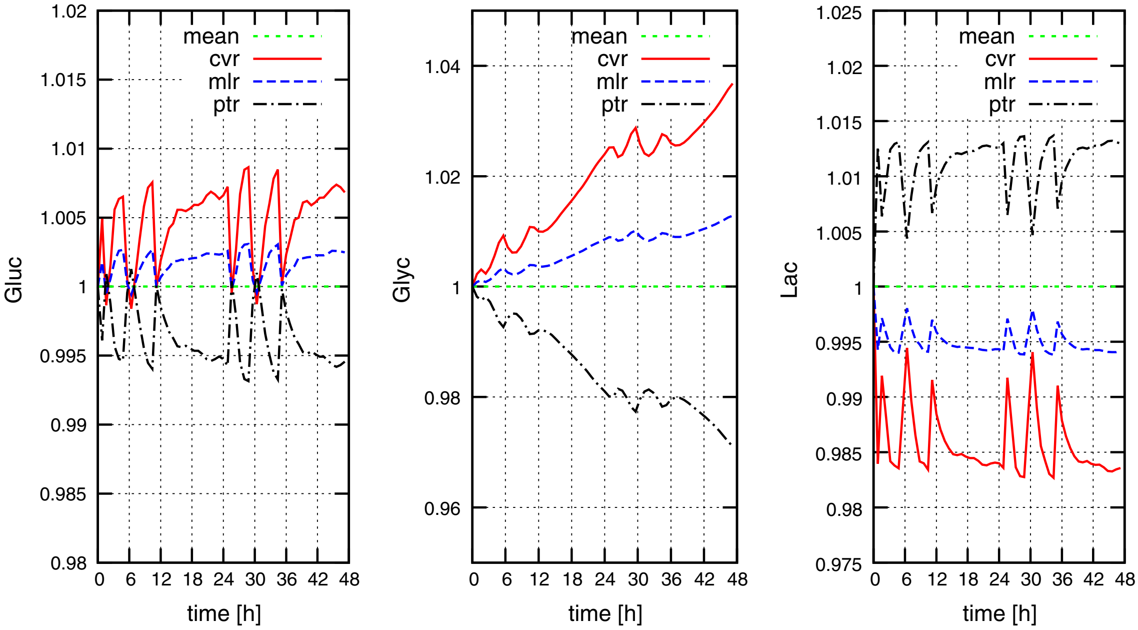

Fig. 14 Evaluation of glucose, glycogen and lactate in the centrilobular, midlobular and periportal region for a three-meal cycle compared with the mean value of the respective concentration in the whole lobule

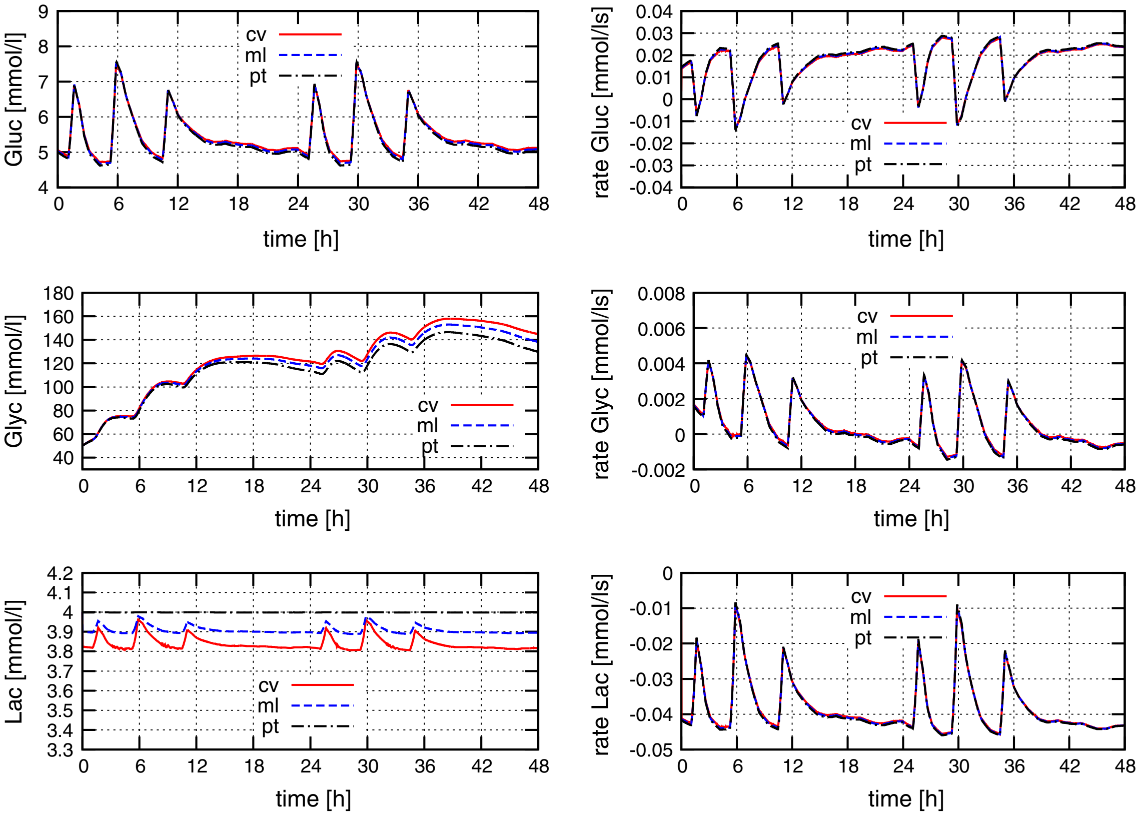

Fig. 15 Evaluation of glucose, glycogen and lactate at three single points along the shortest path between the periportal triad and the central vein for the case of three-meal cycle. One point is located at the central vein (cv), the second is located midlobular (ml) and the third at the portal triad (pt)

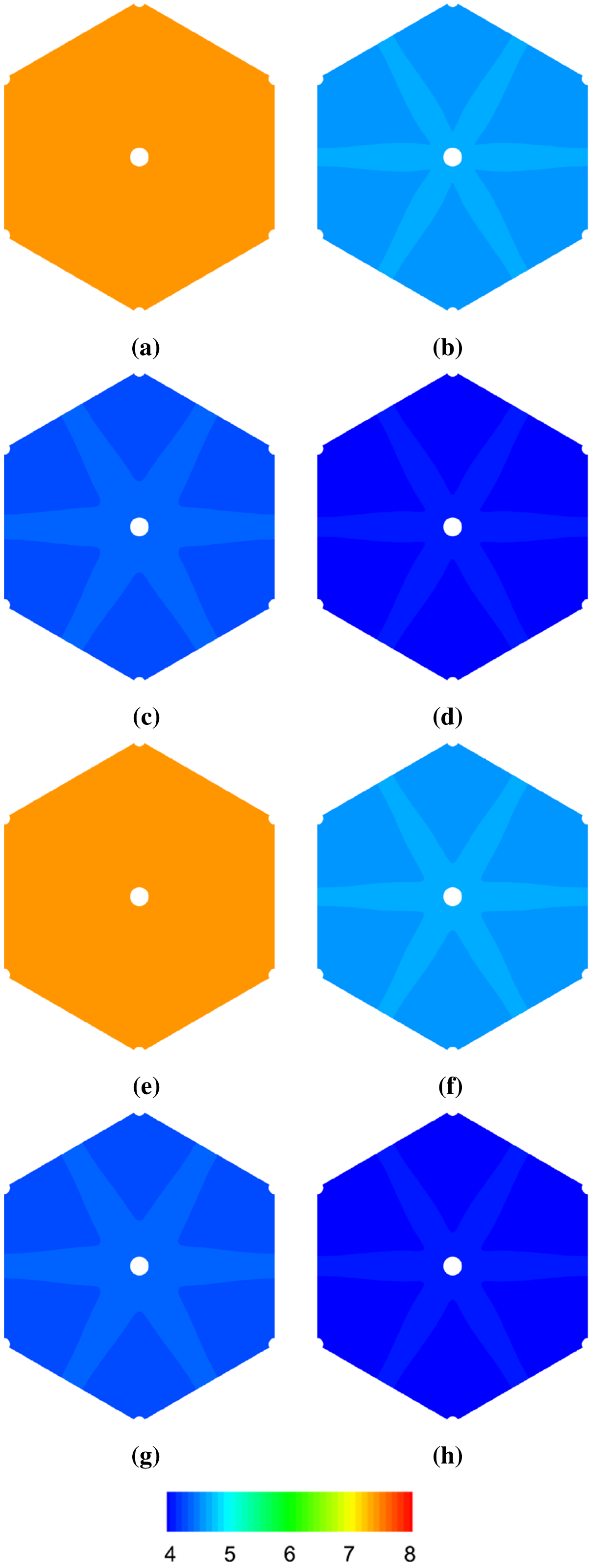

Fig. 16 Contour plots showing the spatial distribution of glucose [mmol/l] taken from a finite element simulation. Applied boundary conditions can be taken from Fig. 8 (one-meal uptake). Loading cycle has been applied twice to match the simulated time of 48 h. **a** 6 h, **b** 12 h, **c** 18 h, **d** 24 h, **e** 30 h, **f** 36 h, **g** 42 h, **h** 48 h

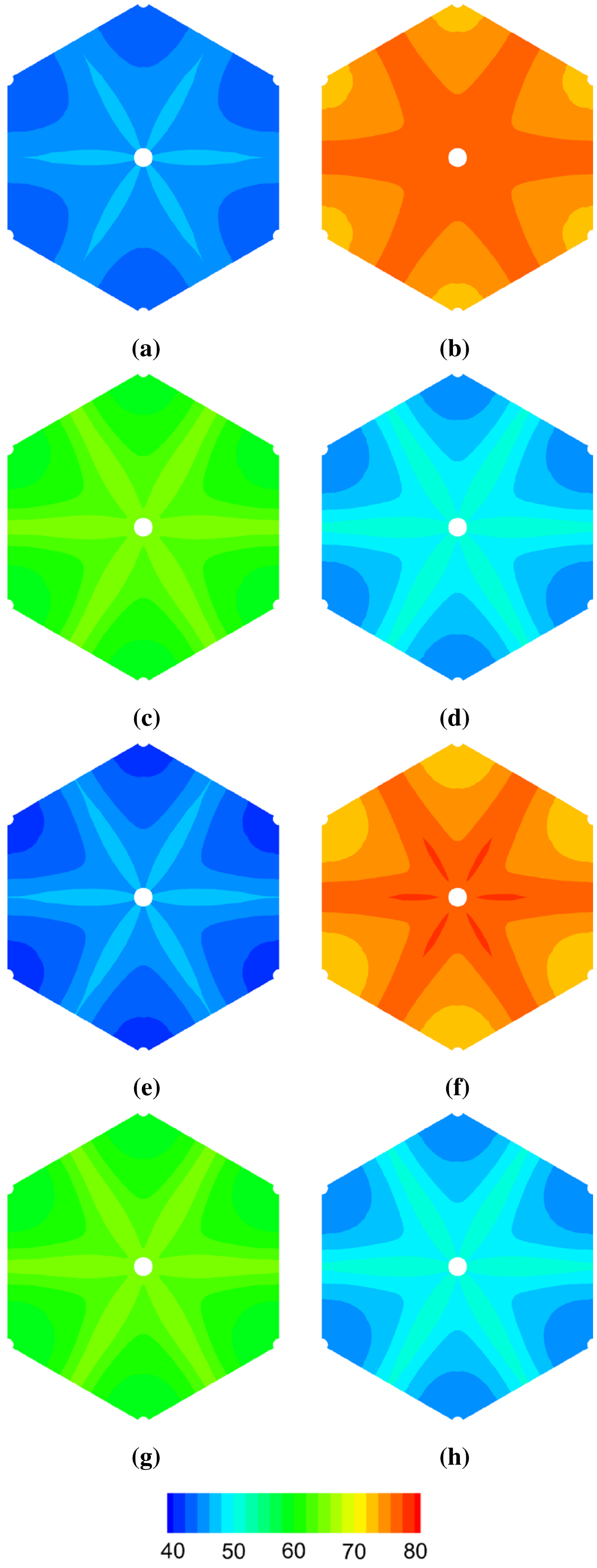

Fig. 17 Contour plots showing the spatial distribution of stored glycogen [mmol/l] taken from a finite element simulation. Applied boundary conditions can be taken from Fig. 8 (one-meal uptake). Loading cycle has been applied twice to match the simulated time of 48 h. **a** 6 h, **b** 12 h, **c** 18 h, **d** 24 h, **e** 30 h, **f** 36 h, **g** 42 h, **h** 48 h

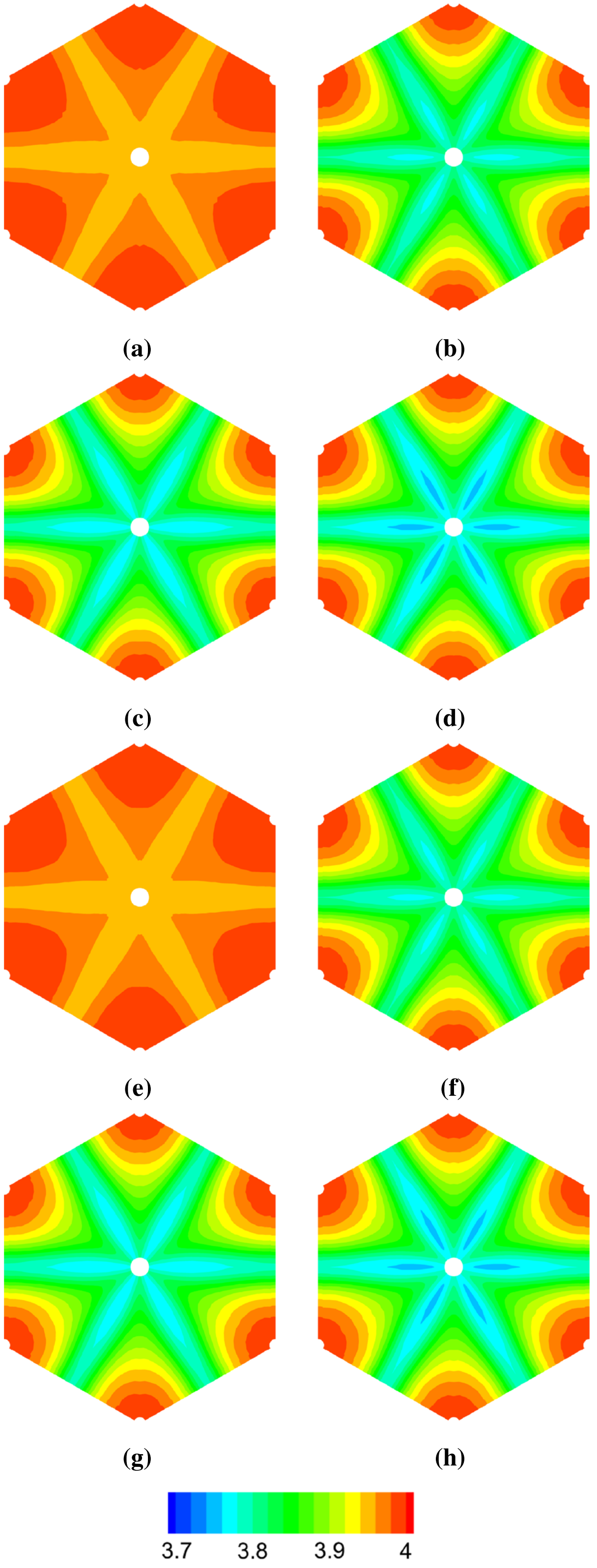
(a) (b) (c) (d) (e) (f) (g) (h)

Fig. 18 Contour plots showing the spatial distribution of lactate [mmol/l] taken from a finite element simulation. Applied boundary conditions can be taken from Fig. 8 (one-meal uptake). Loading cycle has been applied twice to match the simulated time of 48 h, **a** 6 h, **b** 12 h, **c** 18 h, **d** 24 h, **e** 30 h, **f** 36 h, **g** 42 h, **h** 48 h

one of the main features of multiscale models (Walpole et al. 2013). In the context of the multiscale modeling, the performed model reduction in a detailed kinetic model to effective equations which still capture the main model behavior made the integration of metabolism into the spatial framework of FEM feasible. Only this reduction in its complexity allowed the effective coupling of the models on different scales. Already with simplified metabolic model of glucose metabolism, our multiscale model is able to reproduce the overall role of the liver in glucose homeostasis as well as spatial effects due to metabolic coupling between the hepatocytes based on established metabolic gradients within the sinusoid.

9.3 Summary and outlook

In this study, the general framework of a two-scale approach has been presented which describes the basic coupled transport–reaction mechanisms between blood perfusion on lobule scale with metabolism on cell scale.

The model on lobule scale is a multicomponent homogenization approach based on the theory of porous media. The model is based on the principles of rational thermodynamics, is energetically consistent, and is formulated in a continuum mechanical framework. The resulting partial differential equations (PDE) are solved numerically by use of the finite element method (FEM). It describes all relevant coupled phenomena, i.e., the transverse isotropically transport of the fluid (driven mainly by the pressure gradient) and the solved species (driven mainly by convection and diffusion), strains and stresses of the solid (less important in this study) as well as all significant interactions and reactions between the phases and components (in particular the transport as well as metabolism driven exchange of glucose, lactate and glycogen).

The homogenized multicomponent lobule model is coupled to the metabolism cell model. The cell model is based on a coupled system of ordinary differential equations (ODE). The metabolism cell model is solved in every gauss point (calculation point of FEM model) and in every time step of the overlaying lobule FEM model. The input boundary conditions (blood concentration of glucose and lactate) of the metabolism cell model are gained from the overlaying lobule FEM model. As an output, the metabolism cell model deliver the metabolism rates for glucose, lactate and glycogen, which are used as input values for the lobule FEM model.

The main objective of this study was to demonstrate that cell metabolism in liver lobules can be modeled in a two-scale approach which includes in principal all relevant transport and reaction quantities. As proof of principle, the temporal and spatial depending deposition and depletion of glycogen in a liver lobule has been simulated. Based on this investigation, further studies will be performed to enlarge the applicability of the model to more realistic metabolism states and finally to liver diseases.

Appendix

Kinematics

The saturated porous solid is treated as an immiscible mixture of all constituents $\varphi^{\boldsymbol{\alpha}}$ with particles $X_{\boldsymbol{\alpha}}$ with an own independent motion function

$$\mathbf{x} = \boldsymbol{\chi}_{\alpha}(\mathbf{X}_{\alpha}, \mathrm{t})\,, \quad \mathbf{X}_{\alpha} = \boldsymbol{\chi}_{\alpha}^{-1}(\mathbf{x}, \mathrm{t})\,. \tag{40}$$

where $(40)_1$ represents the Lagrange description of motion. The function $\boldsymbol{\chi}_{\alpha}$ is postulated to be unique and uniquely invertible at any time t. The existence of a function inverse to $(40)_1$ leads to the Euler description of motion, see $(40)_2$. A mathematical condition, which is necessary and sufficient for the existence of equation $(40)_2$, is given if the Jacobian $\mathrm{J}_{\alpha} = \det \mathbf{F}_{\alpha}$ differs from zero. Therein, $\mathbf{F}_{\alpha}$ is the deformation gradient. The tensor $\mathbf{F}_{\alpha}$ and its inverse $\mathbf{F}_{\alpha}^{-1}$ are defined as $\mathbf{F}_{\alpha} = \partial \mathbf{x} / \partial \mathbf{X}_{\alpha} = \mathrm{Grad}_{\alpha}\, \boldsymbol{\chi}_{\alpha}$ and $\mathbf{F}_{\alpha}^{-1} = \partial \mathbf{X}_{\alpha} / \partial \mathbf{x} = \mathrm{grad}\, \mathbf{X}_{\alpha}$. The differential operator "Grad_{α}" is referring to a partial differentiation with respect to the reference position $\mathbf{X}_{\alpha}$ of the constituent $\varphi^{\boldsymbol{\alpha}}$ and the differential operator "grad" referring to the spatial point $\mathbf{x}$. During the deformation process, $\mathbf{F}_{\alpha}$ is restricted to $\det \mathbf{F}_{\alpha} > 0$. The spatial velocity gradient $\mathbf{L}_{\alpha} = (\mathrm{Grad}_{\alpha}\, \mathbf{x}'_{\alpha})\, \mathbf{F}_{\alpha}^{-1} = \mathrm{grad}\, \mathbf{x}'_{\alpha}$, where $(\mathbf{F}_{\alpha})'_{\alpha} = \partial \mathbf{x}'_{\alpha} / \partial \mathbf{X}_{\alpha} = \mathrm{Grad}_{\alpha}\, \mathbf{x}'_{\alpha}$ denotes the material velocity gradient, can be additively decomposed into a symmetric part $\mathbf{D}_{\alpha} = (\mathbf{L}_{\alpha} + \mathbf{L}_{\alpha}^{\mathrm{T}})\,/\,2$ and a skew-symmetric part $\mathbf{W}_{\alpha} = (\mathbf{L}_{\alpha} - \mathbf{L}_{\alpha}^{\mathrm{T}})\,/\,2$ with $\mathbf{L}_{\alpha} = \mathbf{D}_{\alpha} + \mathbf{W}_{\alpha}$.

With the Lagrange description of motion $(40)_1$, the velocity and acceleration fields of the constituents $\varphi^{\boldsymbol{\alpha}}$ are defined as material time derivatives of the motion function $(40)_1$, see Fig. 19,

$$\mathbf{x}'_{\alpha} = \frac{\partial \boldsymbol{\chi}_{\alpha}(\mathbf{X}_{\alpha}, \mathrm{t})}{\partial \mathrm{t}}\,, \quad \mathbf{x}''_{\alpha} = \frac{\partial^2 \boldsymbol{\chi}_{\alpha}(\mathbf{X}_{\alpha}, \mathrm{t})}{\partial \mathrm{t}^2}\,. \tag{41}$$

For scalar fields depending on $\mathbf{x}$ and t, the material time derivatives are defined as

$$(\ldots)'_{\alpha} = \partial(\ldots)/\partial \mathrm{t} + \mathrm{grad}\,(\ldots) \cdot \mathbf{x}'_{\alpha}, \tag{42}$$

see, e.g., de Boer (2000).

Constitutive theory

With respect to the assumptions made in Sect. 3, the material time derivative of the saturation condition (24) is an equation in excess that restricts the motion of the incompressible constituents. Therefore, the set of unknown field quantities must be extended by a scalar, namely the Lagrange multiplier $\bar{\lambda}$, which is understood as an indeterminate reaction force due to the saturation condition. Thus, the set of unknown field quantities is:

$$\mathcal{U} = \{\, \boldsymbol{\chi}_{\alpha},\ \mathrm{c}^{\alpha\beta},\ \bar{\lambda} \,\} \tag{43}$$

Considering that the external acceleration $\mathbf{b}$, i.e., the acceleration of gravity, is known, the remaining quantities

$$\mathcal{C} = \left\{ \mathbf{T}^{\boldsymbol{\alpha}},\ \hat{\mathbf{p}}^{\mathrm{F}},\ \hat{\mathbf{p}}^{\alpha\beta},\ \hat{\mathrm{c}}^{\alpha\beta} \right\} \tag{44}$$

in the set of field equations, see Sect. 4, require constitutive relations in order to close the system of equations. In view of the treatment of the entropy inequality in analogy to Coleman and Noll (1963) the following set of free but not overall independent process variables is chosen:

$$\begin{aligned} \mathcal{P} = \Big\{ & \mathbf{C}_{\mathrm{S}}, \mathrm{n}^{\mathrm{S}}, \mathrm{n}^{\mathrm{F}}, \mathbf{w}_{\mathrm{FS}}, \mathbf{w}_{\mathrm{F}\beta S}, \mathrm{c}^{\mathrm{S}\beta}, \mathrm{c}^{\mathrm{F}\beta}, \mathrm{grad}\mathrm{n}^{\mathrm{F}}, \\ & \mathrm{grad}\mathrm{c}^{\mathrm{S}\beta}, \mathrm{grad}\mathrm{c}^{\mathrm{F}\beta} \Big\} \end{aligned} \tag{45}$$

In (45) the right Cauchy-Green deformation tensor $\mathbf{C}_{\mathrm{S}} = \mathbf{F}_{\mathrm{S}}^{\mathrm{T}}\, \mathbf{F}_{\mathrm{S}}$ is considered. The entropy inequality for the mixture body

$$\begin{aligned} \sum_{\boldsymbol{\alpha}}^{\mathrm{S,F},\alpha\beta} \Big\{ & -\rho^{\boldsymbol{\alpha}}\, (\psi^{\boldsymbol{\alpha}})'_{\alpha} - \hat{\rho}^{\boldsymbol{\alpha}}\, (\, \psi^{\boldsymbol{\alpha}} - \frac{1}{2}\, \mathbf{x}'_{\alpha} \cdot \mathbf{x}'_{\alpha}\,) \\ & + \mathbf{T}^{\boldsymbol{\alpha}} \cdot \mathbf{D}_{\alpha} + \hat{\mathrm{e}}^{\boldsymbol{\alpha}} - \hat{\mathbf{p}}^{\boldsymbol{\alpha}} \cdot \mathbf{x}'_{\alpha} \,\Big\} \geq 0 \end{aligned} \tag{46}$$

will be rearranged to ensure no neglecting of dependencies which can influence constitutive modeling. In order to keep the complexity of the evaluation in a justifiable scope, the dependency of the Helmholtz free energies $\psi^{\boldsymbol{\alpha}}$ on the process variables $\mathcal{P}$ will be restricted as follows:

$$\psi^{\mathrm{S}} = \psi^{\mathrm{S}}\,\{\,\mathbf{C}_{\mathrm{S}}\,\}\,, \quad \psi^{\mathrm{F}} = \psi^{\mathrm{F}}\,\{\,-\,\}\,, \quad \psi^{\alpha\beta} = \psi^{\alpha\beta}\,\{\,\mathrm{c}^{\alpha\beta}\,\}\,. \tag{47}$$

For further investigations, the relations $\rho^{\boldsymbol{\alpha}}\, (\psi^{\boldsymbol{\alpha}})'_{\alpha}$ will be replaced by

$$\begin{aligned} \rho^{\mathrm{S}}\, (\psi^{\mathrm{S}})'_{\mathrm{S}} &= 2\, \mathrm{n}^{\mathrm{S}}\, \rho^{\mathrm{SR}}\, \mathbf{F}_{\mathrm{S}}\, \frac{\partial \psi^{\mathrm{S}}}{\partial \mathbf{C}_{\mathrm{S}}}\, \mathbf{F}_{\mathrm{S}}^{\mathrm{T}} \cdot \mathbf{D}_{\mathrm{S}}, \\ \rho^{\mathrm{F}}\, (\psi^{\mathrm{F}})'_{\mathrm{F}} &= 0, \\ \rho^{\alpha\beta}\, (\psi^{\alpha\beta})'_{\beta} &= \rho^{\alpha\beta}\, \frac{\partial \psi^{\alpha\beta}}{\partial \mathrm{c}^{\alpha\beta}}\, (\mathrm{c}^{\alpha\beta})'_{\beta}\,. \end{aligned} \tag{48}$$

For saturated porous media consisting of incompressible constituents the saturation condition (20) is a constraint with respect to the overall volumetric deformation. Therefore, the saturation condition must be considered in view of the evaluation of the entropy inequality. Here, the material time derivative of the saturation condition following the motion of the solid phase with

$$(\mathrm{n}^{\mathrm{S}})'_{\mathrm{S}} + (\mathrm{n}^{\mathrm{F}})'_{\mathrm{S}} = (\mathrm{n}^{\mathrm{S}})'_{\mathrm{S}} + (\mathrm{n}^{\mathrm{F}})'_{\mathrm{F}} - \mathrm{grad}\, \mathrm{n}^{\mathrm{F}} \cdot \mathbf{w}_{\mathrm{FS}} = 0 \tag{49}$$

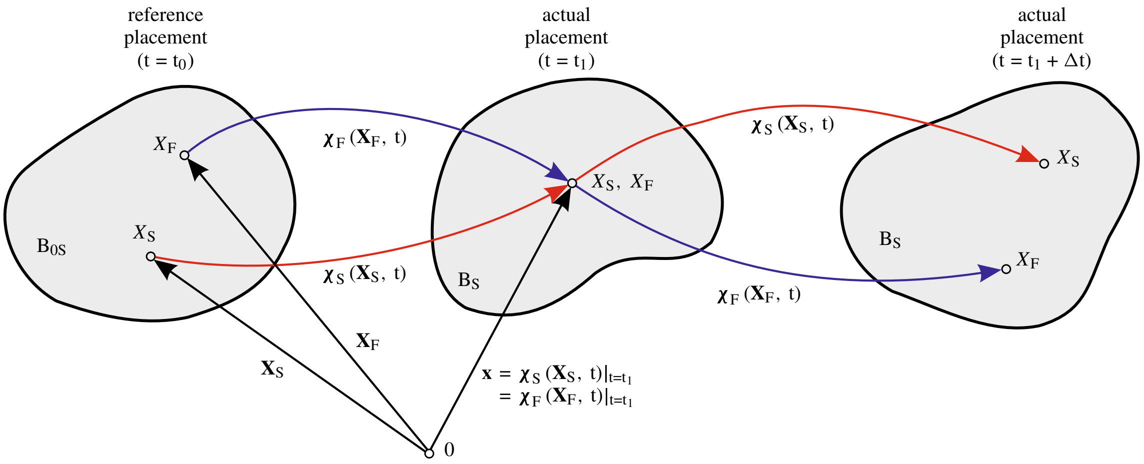

Fig. 19 Motion of solid and fluid particle in a fluid saturated porous solid

will be considered, where (42) and the difference velocity

$$\mathbf{w}_{FS} = \mathbf{x}'_F - \mathbf{x}'_S \tag{50}$$

are used. Applying the identity

$$\begin{aligned}(n^\alpha)'_\alpha &= \frac{n^\alpha}{\rho^\alpha}(\rho^\alpha)'_\alpha - \frac{n^\alpha}{\rho^{\alpha R}}(\rho^\alpha)'_\alpha \\ &= -n^\alpha(\mathbf{D}_\alpha \cdot \mathbf{I}) - \frac{n^\alpha}{\rho^{\alpha R}}\underbrace{(\rho^{\alpha R})'_\alpha}_{=0}, \\ &= -n^\alpha(\mathbf{D}_\alpha \cdot \mathbf{I})\end{aligned} \tag{51}$$

the rate of the saturation condition (49) can be rearranged to

$$n^S(\mathbf{D}_S \cdot \mathbf{I}) + n^F(\mathbf{D}_F \cdot \mathbf{I}) + \operatorname{grad} n^F \cdot \mathbf{w}_{FS} = 0. \tag{52}$$

In view of the constitutive modeling, we use the concept of Lagrange multipliers. Using the identity div $\mathbf{x}'_\alpha = \mathbf{D}_\alpha \cdot \mathbf{I}$, we add $(21)_{1,2}$ to the entropy inequality (46), multiplied by the Lagrange multiplier $\bar{\lambda}$, cf. de Boer (1996). The interconnection between the spatial velocity deformation gradients $\mathbf{D}_\alpha$ with the volume fractions and their material time derivative n^α and $(n^\alpha)'_\alpha$ as well as the mass supplies $\hat{\rho}^\alpha$ will be considered with the balance equations of mass $(14)_1$ multiplied with a respective Lagrange multiplier:

$$\begin{aligned}&\bar{\lambda}^S\left[(n^S)'_S + n^S(\mathbf{D}_S \cdot \mathbf{I})\right] = 0 \\ &\bar{\lambda}^F\left[(n^F)'_F + n^F(\mathbf{D}_F \cdot \mathbf{I})\right] = 0 \\ &\bar{\lambda}^{S\beta}\left[(n^S)'_S\, c^{S\beta} + n^S(c^{S\beta})'_S + n^S c^{S\beta}\,\mathbf{D}_S \cdot \mathbf{I} - \hat{c}^{S\beta}\right] = 0 \\ &\bar{\lambda}^{F\beta}\Big[(n^F)'_F\, c^{F\beta} + n^F(c^{F\beta})'_\beta + \operatorname{grad} n^F(\mathbf{w}_{F\beta S} - \mathbf{w}_{FS})\, c^{F\beta} \\ &\quad + n^F c^{F\beta}\,\mathbf{D}_{F\beta} \cdot \mathbf{I} - \hat{c}^{F\beta}\Big] = 0 \\ &-\bar{\lambda}\left[-n^S\,\mathbf{D}_S \cdot \mathbf{I} - n^F\,\mathbf{D}_F \cdot \mathbf{I} - \operatorname{grad} n^F\,\mathbf{w}_{FS}\right] = 0\end{aligned} \tag{53}$$

The entropy inequality (46), supplemented with the material time derivative of the saturation condition $(53)_5$ and the balance equations of mass $(53)_{1-4}$, all multiplied with the corresponding Lagrange multiplier, reads

$$\begin{aligned}&\mathbf{D}_S \cdot \Big\{\mathbf{T}^S + \mathbf{T}^{S\beta} - 2\,n^S \rho^{SR}\,\mathbf{F}_S \frac{\partial \psi^S}{\partial \mathbf{C}_S}\mathbf{F}_S^T \\ &\quad + \bar{\lambda}\,n^S\,\mathbf{I} + \bar{\lambda}^S n^S\,\mathbf{I} + \bar{\lambda}^{S\beta} c^{S\beta} n^S\,\mathbf{I}\Big\} \\ &\quad + \mathbf{D}_F \cdot \Big\{\mathbf{T}^F + \bar{\lambda}\,n^F\,\mathbf{I} + \bar{\lambda}^F n^F\,\mathbf{I}\Big\} \\ &\quad + \mathbf{D}_{F\beta} \cdot \Big\{\mathbf{T}^{F\beta} + \bar{\lambda}^{F\beta} n^F c^{F\beta}\,\mathbf{I}\Big\} \\ &\quad - (n^S)'_S\Big\{-\bar{\lambda}^S - \bar{\lambda}^{S\beta} c^{S\beta}\Big\} - (n^F)'_F\Big\{-\bar{\lambda}^F - \bar{\lambda}^{F\beta} c^{F\beta}\Big\} \\ &\quad - (c^{F\beta})'_\beta\Big\{\rho^{F\beta}\frac{\partial \psi^{F\beta}}{\partial c^{F\beta}} - \bar{\lambda}^{F\beta} n^F\Big\} \\ &\quad - (c^{S\beta})'_\beta\Big\{\rho^{S\beta}\frac{\partial \psi^{S\beta}}{\partial c^{S\beta}} - \bar{\lambda}^{S\beta} n^S\Big\} \\ &\quad - \hat{\rho}^{S\beta}\Big\{\psi^{S\beta} - \frac{1}{2}\mathbf{x}'_S \cdot \mathbf{x}'_S + \frac{\bar{\lambda}^{S\beta}}{M^\beta_{mol}}\Big\} \\ &\quad - \hat{\rho}^{F\beta}\Big\{\psi^{F\beta} - \frac{1}{2}\mathbf{x}'_{F\beta} \cdot \mathbf{x}'_{F\beta} + \frac{\bar{\lambda}^{F\beta}}{M^\beta_{mol}}\Big\} \\ &\quad - \mathbf{w}_{FS} \cdot \Big\{\hat{\mathbf{p}}^F - \bar{\lambda}\operatorname{grad} n^F + \bar{\lambda}^{F\beta} c^{F\beta}\operatorname{grad} n^F\Big\} \\ &\quad - \mathbf{w}_{F\beta S} \cdot \Big\{\hat{\mathbf{p}}^{F\beta} - \bar{\lambda}^{F\beta} c^{F\beta}\operatorname{grad} n^F\Big\} \geq 0\,,\end{aligned} \tag{54}$$

where use has been made of $\sum \rho^{\alpha\beta} = 0$ and $\hat{\mathbf{p}}^S = -\hat{\mathbf{p}}^F - \hat{\mathbf{p}}^{S\beta} - \hat{\mathbf{p}}^{F\beta}$, see (19). The inequality must hold for fixed values of the process variables, see (45), and for arbitrary values of the so-called free-available quantities $\mathcal{A} = \{\mathbf{D}_\alpha,\ (n^\alpha)'_\alpha,\ (c^{\alpha\beta})'_{\alpha\beta}\}$ which contains selective derivatives of the values contained in $\mathcal{P}$. Thus, the entropy inequality (54) can be satisfied if the following structure is obtained:

$$
\begin{aligned}
&\mathbf{D}_{\mathrm{S}} \cdot \left\{\underbrace{(\dots)}_{=\mathbf{0}}\right\} + \mathbf{D}_{\mathrm{F}} \cdot \left\{\underbrace{(\dots)}_{=\mathbf{0}}\right\} + \mathbf{D}_{\mathrm{F}\beta} \cdot \left\{\underbrace{(\dots)}_{=\mathbf{0}}\right\} \\
&-(\mathrm{n}^{\mathrm{S}})'_{\mathrm{S}} \left\{\underbrace{(\dots)}_{=0}\right\} - (\mathrm{n}^{\mathrm{F}})'_{\mathrm{F}} \left\{\underbrace{(\dots)}_{=0}\right\} \\
&-(\mathrm{c}^{\mathrm{S}\beta})'_{\mathrm{S}\beta} \left\{\underbrace{(\dots)}_{=0}\right\} - (\mathrm{c}^{\mathrm{F}\beta})'_{\mathrm{F}\beta} \{\underbrace{(\dots)}_{=0}\} + \underbrace{\mathcal{D}is}_{\geq 0} \geq 0\,,
\end{aligned}
\tag{55}
$$

where the dissipation mechanism

$$
\begin{aligned}
\mathcal{D}is = &-\hat{\rho}^{\mathrm{S}\beta} \left\{ \psi^{\mathrm{S}\beta} - \frac{1}{2}\,\mathbf{x}'_{\mathrm{S}} \cdot \mathbf{x}'_{\mathrm{S}} + \frac{\bar{\lambda}^{\mathrm{S}\beta}}{\mathrm{M}^{\beta}_{\mathrm{mol}}} \right\} \\
&-\hat{\rho}^{\mathrm{F}\beta} \left\{ \psi^{\mathrm{F}\beta} - \frac{1}{2}\,\mathbf{x}'_{\mathrm{F}\beta} \cdot \mathbf{x}'_{\mathrm{F}\beta} + \frac{\bar{\lambda}^{\mathrm{F}\beta}}{\mathrm{M}^{\beta}_{\mathrm{mol}}} \right\} \\
&-\mathbf{w}_{\mathrm{FS}} \cdot \left\{ \hat{\mathbf{p}}^{\mathrm{F}} - \bar{\lambda}\ \mathrm{grad}\ \mathrm{n}^{\mathrm{F}} + \bar{\lambda}^{\mathrm{F}\beta}\,\mathrm{c}^{\mathrm{F}\beta}\ \mathrm{grad}\ \mathrm{n}^{\mathrm{F}} \right\} \\
&-\mathbf{w}_{\mathrm{F}\beta\mathrm{S}} \cdot \{ \hat{\mathbf{p}}^{\mathrm{F}\beta} - \bar{\lambda}^{\mathrm{F}\beta}\,\mathrm{c}^{\mathrm{F}\beta}\ \mathrm{grad}\ \mathrm{n}^{\mathrm{F}} \} \geq 0
\end{aligned}
\tag{56}
$$

must hold. Considering the aforementioned remarks, we obtain necessary and sufficient conditions for the unrestricted validity of the second law of thermodynamics. The Lagrange multipliers associated with the solutes can be identified from (55), terms 4–7, as

$$
\begin{aligned}
\bar{\lambda}^{\alpha} &= -\bar{\lambda}^{\alpha\beta}\,\mathrm{c}^{\alpha\beta}, \\
\bar{\lambda}^{\alpha\beta} &= \frac{\rho^{\alpha\beta}}{\mathrm{n}^{\alpha}}\,\frac{\partial\psi^{\alpha\beta}}{\partial\mathrm{c}^{\alpha\beta}} = \mathrm{c}^{\alpha\beta}\,\mathrm{M}^{\beta}_{\mathrm{mol}}\,\frac{\partial\psi^{\alpha\beta}}{\partial\mathrm{c}^{\alpha\beta}}.
\end{aligned}
\tag{57}
$$

Thus, we obtain from (55), terms 1–3 for the Cauchy stress tensors

$$
\begin{aligned}
\mathbf{T}^{\mathbf{S}} &= \mathbf{T}^{\mathrm{S}} + \mathbf{T}^{\mathrm{S}\beta} \\
&= -\bar{\lambda}\,\mathrm{n}^{\mathrm{S}}\,\mathbf{I}\ \underbrace{-\bar{\lambda}^{\mathrm{S}}\,\mathrm{n}^{\mathrm{S}}\,\mathbf{I} - \bar{\lambda}^{\mathrm{S}\beta}\mathrm{c}^{\mathrm{S}\beta}\,\mathrm{n}^{\mathrm{S}}\,\mathbf{I}}_{=0} + 2\,\rho^{\mathrm{S}}\,\mathbf{F}_{\mathrm{S}}\,\frac{\partial\psi^{\mathrm{S}}}{\partial\mathbf{C}_{\mathrm{S}}}\,\mathbf{F}^{\mathrm{T}}_{\mathrm{S}} \\
&= -\bar{\lambda}\,\mathrm{n}^{\mathrm{S}}\,\mathbf{I} + \underbrace{2\,\rho^{\mathrm{S}}\,\mathbf{F}_{\mathrm{S}}\,\frac{\partial\psi^{\mathrm{S}}}{\partial\mathbf{C}_{\mathrm{S}}}\,\mathbf{F}^{\mathrm{T}}_{\mathrm{S}}}_{\mathbf{T}^{\mathbf{S}}_{\mathrm{E}}}\,, \\
\mathbf{T}^{\mathrm{F}} &= +\bar{\lambda}\,\mathrm{n}^{\mathrm{F}}\,\mathbf{I} + \bar{\lambda}^{\mathrm{F}}\,\mathrm{n}^{\mathrm{F}}\,\mathbf{I} \\
&= -\bar{\lambda}\,\mathrm{n}^{\mathrm{F}}\,\mathbf{I} + \mathrm{n}^{\mathrm{F}}\,(\mathrm{c}^{\mathrm{F}\beta})^2\mathrm{M}^{\beta}_{\mathrm{mol}}\,\frac{\partial\psi^{\mathrm{F}\beta}}{\partial\mathrm{c}^{\mathrm{F}\beta}}\,\mathbf{I}\,, \\
\mathbf{T}^{\mathrm{F}\beta} &= -\bar{\lambda}^{\mathrm{F}\beta}\,\mathrm{n}^{\mathrm{F}}\,\mathrm{c}^{\mathrm{F}\beta}\,\mathbf{I} \\
&= -\,\mathrm{n}^{\mathrm{F}}\,(\mathrm{c}^{\mathrm{F}\beta})^2\,\mathrm{M}^{\beta}_{\mathrm{mol}}\,\frac{\partial\psi^{\mathrm{F}\beta}}{\partial\mathrm{c}^{\mathrm{F}\beta}}\,\mathbf{I} \\
&= -\mathrm{n}^{\mathrm{F}}\,\mu^{\mathrm{F}\beta}\,\mathbf{I}\,,
\end{aligned}
\tag{58}
$$

using $(57)_{1,2}$ and the abbreviations $\mathbf{T}^{\mathbf{S}} = \mathbf{T}^{\mathrm{S}} + \mathbf{T}^{\mathrm{S}\beta}$ for the overall solid stress and $\mu^{\mathrm{F}\beta} = (\mathrm{c}^{\mathrm{F}\beta})^2\,\mathrm{M}^{\beta}_{\mathrm{mol}}\,(\partial\psi^{\mathrm{F}\beta}/\partial\mathrm{c}^{\mathrm{F}\beta})$ for the chemical potential. Moreover, the Lagrange multiplier $\bar{\lambda}$ is understood as the reaction force between the solid and fluid phase, which can be identify as the pore pressure λ with $\bar{\lambda} = \lambda$, cf. eg. Bluhm (2002). In view of the dissipative mechanism (56), the following approaches for the interaction forces $\hat{\mathbf{p}}^{\mathrm{F}}$ and $\hat{\mathbf{p}}^{\mathrm{F}\beta}$ and for the mass supply $\rho^{\alpha\beta}$ are postulated:

$$
\begin{aligned}
\hat{\mathbf{p}}^{\mathrm{F}} &= \bar{\lambda}\ \mathrm{grad}\ \mathrm{n}^{\mathrm{F}} - \bar{\lambda}^{\mathrm{F}\beta}\,\mathrm{c}^{\mathrm{F}\beta}\ \mathrm{grad}\ \mathrm{n}^{\mathrm{F}} - \alpha_{\mathbf{w}_{\mathrm{FS}}}\,\mathbf{w}_{\mathrm{FS}} \\
&\quad + \alpha_{\mathbf{w}_{\mathrm{FF}\beta}}\,\mathbf{w}_{\mathrm{FF}\beta}\,, \\
\hat{\mathbf{p}}^{\mathrm{F}\beta} &= \bar{\lambda}^{\mathrm{F}\beta}\,\mathrm{c}^{\mathrm{F}\beta}\ \mathrm{grad}\ \mathrm{n}^{\mathrm{F}} - \alpha_{\mathbf{w}_{\beta\mathrm{S}}}\,\mathbf{w}_{\beta\mathrm{S}} - \alpha_{\mathbf{w}_{\mathrm{FF}\beta}}\,\mathbf{w}_{\mathrm{FF}\beta}\,, \\
\hat{\rho}^{\mathrm{FLc}} &= -\delta^{\mathrm{FLc}}(\Psi^{\mathrm{FLc}} - \Psi^{\mathrm{SGy}})\,, \\
\hat{\rho}^{\mathrm{FGu}} &= -\delta^{\mathrm{FGu}}(\Psi^{\mathrm{FGu}} - \Psi^{\mathrm{SGy}})\,,
\end{aligned}
\tag{59}
$$

with the abbreveation $\Psi^{\alpha\beta} = \psi^{\alpha\beta} - 1/2\,\mathbf{x}'_{\alpha\beta} \cdot \mathbf{x}'_{\alpha\beta} + \bar{\lambda}^{\alpha\beta}/\mathrm{M}^{\beta}_{\mathrm{mol}}$. The factors connected to the relative permeabilities $\alpha_{\mathbf{w}_{\mathrm{FS}}}$, $\alpha_{\mathbf{w}_{\mathrm{FF}\beta}}$, $\alpha_{\mathbf{w}_{\beta\mathrm{S}}}$ and connected to the mass supply terms δ^{FLc}, δ^{FGu} are material parameters depending on the set $\mathcal{U}$ given in (43) and are restricted to positive values (≥ 0).

Regarding the liver lobe level (microperfusion scale), we receive constitutive restrictions with respect to the concentration exchange of lactate and glucose from $(59)_{3,4}$ with

$$
\begin{aligned}
\hat{\rho}^{\mathrm{FLc}} &= \mathrm{M}^{\mathrm{Lc}}_{\mathrm{mol}}\,\hat{\mathrm{c}}^{\mathrm{FLc}} = -\delta^{\mathrm{FLc}}(\Psi^{\mathrm{FLc}} - \Psi^{\mathrm{SGy}})\,, \\
\hat{\rho}^{\mathrm{FGu}} &= \mathrm{M}^{\mathrm{Gu}}_{\mathrm{mol}}\,\hat{\mathrm{c}}^{\mathrm{FGu}} = -\delta^{\mathrm{FGu}}(\Psi^{\mathrm{FGu}} - \Psi^{\mathrm{SGy}})\,,
\end{aligned}
\tag{60}
$$

where $\Psi^{\alpha\beta} = \psi^{\alpha\beta} - 1/2\,\mathbf{x}'_{\alpha\beta} \cdot \mathbf{x}'_{\alpha\beta} + (\bar{\lambda}^{\alpha\beta}/\mathrm{M}^{\beta}_{\mathrm{mol}})$. We assume now that the concentration exchange depends neither on kinetic energy $1/2\ \mathbf{x}'_{\alpha\beta} \cdot \mathbf{x}'_{\alpha\beta}$ nor on the pressure state $\bar{\lambda}^{\alpha\beta}$. Thus, the concentration exchange rates reduce with (18) to

$$
\begin{aligned}
\hat{\mathrm{c}}^{\mathrm{FLc}} &= \frac{\hat{\rho}^{\mathrm{FLc}}}{\mathrm{M}^{\mathrm{Lc}}_{\mathrm{mol}}} = -\frac{\delta^{\mathrm{FLc}}}{\mathrm{M}^{\mathrm{Lc}}_{\mathrm{mol}}}(\psi^{\mathrm{FLc}} - \psi^{\mathrm{SGy}})\,, \\
\hat{\mathrm{c}}^{\mathrm{FGu}} &= \frac{\hat{\rho}^{\mathrm{FGu}}}{\mathrm{M}^{\mathrm{Gu}}_{\mathrm{mol}}} = -\frac{\delta^{\mathrm{FGu}}}{\mathrm{M}^{\mathrm{Gu}}_{\mathrm{mol}}}(\psi^{\mathrm{FGu}} - \psi^{\mathrm{SGy}})\,, \\
\hat{\mathrm{c}}^{\mathrm{SGy}} &= -\hat{\mathrm{c}}^{\mathrm{FLc}} - \hat{\mathrm{c}}^{\mathrm{FGu}}.
\end{aligned}
\tag{61}
$$

Derivation of field equations

Considering that the solid and fluid carrier phases are treated to be material incompressible ($(\rho^{\alpha\mathrm{R}})'_{\alpha} = 0$), see Sec. 3, leads to the simplification

$$
(\rho^{\alpha})'_{\alpha} = (\mathrm{n}^{\alpha}\,\rho^{\alpha\mathrm{R}})'_{S} = (\mathrm{n}^{\alpha})'_{\alpha}\,\rho^{\alpha R} + \mathrm{n}^{\alpha}\,\underbrace{(\rho^{\alpha R})}_{=0} = (\mathrm{n}^{\alpha})'_{\alpha}\,\rho^{\alpha R}.
\tag{62}
$$

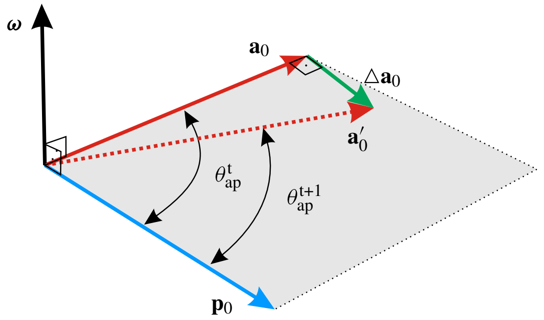

Fig. 20 Developing different angel $\theta_{\mathrm{ap}}^{\mathrm{t}}$ in the $\mathbf{a}_0 \times \mathbf{p}_0$ plain spanned by the pressure gradient $\mathbf{p}_0$ and preferred flow direction $\mathbf{a}_0$ or $\mathbf{a}_0'$

Incorporating additionally that mass exchanges are only acts between the solute ($\hat{\rho}^\alpha = 0$), the balance equation of mass $(14)_1$ reduce for the solid and fluid carrier phases to

$$(\mathrm{n}^{\mathrm{S}})'_{\mathrm{S}} + \mathrm{n}^{\mathrm{S}} \operatorname{div} \mathbf{x}'_{\mathrm{S}} = 0\,, \quad (\mathrm{n}^{\mathrm{F}})'_{\mathrm{F}} + \mathrm{n}^{\mathrm{F}} \operatorname{div} \mathbf{x}'_{\mathrm{F}} = 0. \tag{63}$$

In addition, with (11) the mass for the solutes is given with

$$\begin{aligned} \mathrm{m}^\beta(\mathbf{x}, \mathrm{t}) &= \int_{\mathrm{M}_\beta} \mathrm{dm}^\beta \\ &= \int_{\mathrm{B}_\alpha} \mathrm{c}^{\alpha\beta}\, \mathrm{M}^\beta_{\mathrm{mol}}\, \mathrm{dv}^\alpha \\ &= \int_{\mathrm{B}_\alpha} \mathrm{n}^\alpha\, \mathrm{c}^{\alpha\beta}\, \mathrm{M}^\beta_{\mathrm{mol}}\, \mathrm{dv}, \end{aligned} \tag{64}$$

which directly leads to the solute balance equation

$$\left(\mathrm{n}^\alpha\, \mathrm{c}^{\alpha\beta}\, \mathrm{M}^\beta_{\mathrm{mol}}\right)'_{\alpha\beta} + \mathrm{n}^\alpha\, \mathrm{c}^{\alpha\beta}\, \mathrm{M}^\beta_{\mathrm{mol}} \operatorname{div} \mathbf{x}'_{\alpha\beta} = \hat{\rho}^{\alpha\beta}. \tag{65}$$

Further, we consider that $\mathrm{M}^\beta_{\mathrm{mol}}$ is a constant of the substance φ^β and applies for the time derivatives for scalar fields (42). Thus, the solute balance equation of mass (65) yields with (13) to

$$(\mathrm{n}^\alpha)'_{\mathrm{S}}\, \mathrm{c}^{\alpha\beta} + \mathrm{n}^\alpha\, (\mathrm{c}^{\alpha\beta})'_{\mathrm{S}} + \operatorname{div}\left(\mathbf{j}^{\alpha\beta}\right) + \mathrm{n}^\alpha\, \mathrm{c}^{\alpha\beta} \operatorname{div} \mathbf{x}'_{\mathrm{S}} = \hat{\mathrm{c}}^{\alpha\beta}. \tag{66}$$

Herein,

$$\mathbf{j}^{\alpha\beta} = \mathrm{c}^{\alpha\beta}\, \mathrm{n}^\alpha\, \mathbf{w}_{\alpha\beta\mathrm{S}} = -\mathrm{D}_{\alpha\beta}\, [-\mathrm{n}^\alpha\, \mathrm{grad}\mathrm{c}^{\alpha\beta}] + \hat{\mathrm{D}}_{\alpha\beta}\, \mathbf{w}_{\alpha\mathrm{S}} \tag{67}$$

denotes the molar flux, with $\mathrm{D}_{\alpha\beta}$ as the diffusion coefficient (Fick's part), $\hat{\mathrm{D}}_{\alpha\beta}$ as the advective coefficient (advective part) and $\mathbf{w}_{\alpha\beta\mathrm{S}} = \mathbf{x}'_{\alpha\beta} - \mathbf{x}'_{\mathrm{S}}$ as the velocity of the solute $\varphi^{\alpha\beta}$ solved in the carrier phase φ^α relative to the solid velocity.

Evolutionary approach for preferred flow direction

The stationary solution for the anisotropic flow is achieved following the phenomenological approach that sinusoids tend to be oriented in the direction of the pressure gradient $\mathbf{p}_0 = \|\mathrm{Grad}\,\bar{\lambda}\|$ with $|\mathbf{p}_0| = 1$; see Fig. 20. Thus, starting from an arbitrary preferred flow direction $\mathbf{a}_0$ with $|\mathbf{a}_0| = 1$ an updated preferred flow direction $\mathbf{a}_0'$ is calculated with the relation

$$\mathbf{a}_0' = \mathbf{a}_0 + \triangle\mathbf{a}_0' \quad \text{with} \quad \mathbf{a}_0 \cdot \triangle\mathbf{a}_0 = 0 \tag{68}$$

where $\triangle\mathbf{a}_0'$ denotes the incremental update of the preferred flow direction $\mathbf{a}_0$ Werner et al. (2012). The incremental update can be expressed by a rigid body rotation of $\mathbf{a}_0$ by $\triangle\mathbf{a}_0 = \boldsymbol{\omega} \times \mathbf{a}_0$ where $\boldsymbol{\omega}$ denotes the angular velocity of reorientation. Since $\boldsymbol{\omega}$ is perpendicular to the plane spanned by $\mathbf{a}_0$ and $\mathbf{p}_0$ the condition $\boldsymbol{\omega} = \frac{\delta_{\mathrm{t}}}{\delta_{\mathrm{d}}}(\mathbf{a}_0 \times \mathbf{p}_0)$ must hold with δ_{t} denoting a virtual damping coefficient with respect to the time-dependent model and $\delta_{\mathrm{d}} = |\mathbf{a}_0 - \mathbf{p}_0|$ weighting the distance between the preferred flow direction and the pressure gradient. Thus, the incremental update reads

$$\triangle\mathbf{a}_0 = \frac{\delta_{\mathrm{t}}}{\delta_{\mathrm{d}}}([\mathbf{a}_0 \times \mathbf{p}_0] \times \mathbf{a}_0). \tag{69}$$

Supplemental information model reduction

V_{liver}	1.5 l	liver volume in full kinetic model
V_{sim}		liver volume for simulation in liter
V_{f}	$\frac{V_{\text{sim}}}{V_{\text{liver}}}$	Relative volume for adaptions of model fluxes and properties like the glycogen storage capacity to the actual liver volume
$C_{\text{HGU}}, C_{\text{GLY}}$		Coefficients for polynomial approximation of quasi-steady state
m_{bw}	75 kg	Body weight used for conversion of fluxes given per body weight in concentration changes
$k_{\text{z}} = k_{\text{x}}$	0.05 mM	Saturation parameter accounting for substrate limitation: HGU and glycolysis are limited by the available φ^{FGu}. HGP and gluconeogenesis are limited by available gluconeogenic substrate (handles the border conditions for integration in the polynoms)

$$x = \varphi^{\text{FGu}}\ y = \frac{\varphi^{\text{SGy}}}{V_f},\ z = \varphi^{\text{FLc}}$$

$$C_{\text{HGU}} = \begin{pmatrix} 0.002037960420379 \\ -0.000367490977632 \\ -0.069301032419012 \\ -0.000002823120484 \\ 0.011282864074433 \\ 3.740276159346358 \\ -0.000000181515364 \\ 0.000157328485157 \\ -0.100050917438436 \\ -18.414978834613287 \end{pmatrix}$$

$$C_{\mathrm{GLY}} = \begin{pmatrix} -0.013260401508103 \\ -0.000078240970095 \\ 0.478235644004833 \\ 0.000002861605817 \\ 0.000932752106971 \\ -2.492569641130055 \\ 0.000000166945924 \\ -0.000125285017396 \\ 0.015354944655784 \\ -4.975026288067225 \end{pmatrix}$$

$$\begin{aligned} & p_{\mathrm{HGU}}(\varphi^{\mathrm{FGu}}, \varphi^{\mathrm{SGy}}, \varphi^{\mathrm{FLc}}) \\ & = \frac{V_{\mathrm{f}}\, m_{\mathrm{bw}}}{60 \cdot 10^{-3}} \cdot (C_{\mathrm{HGU}}[1] \cdot x^3 + C_{\mathrm{HGU}}[2] \cdot x^2 \mathrm{y} \\ & + C_{\mathrm{HGU}}[3] \cdot x^2 + C_{\mathrm{HGU}}[4] \cdot x y^2 + C_{\mathrm{HGU}}[5] \cdot x y \\ & + C_{\mathrm{HGU}}[6] \cdot x + C_{\mathrm{HGU}}[7] \cdot y^3 + C_{\mathrm{HGU}}[8] \cdot y^2 \\ & + C_{\mathrm{HGU}}[9] \cdot y + C_{\mathrm{HGU}}[10]) \end{aligned} \tag{70}$$

$$\begin{aligned} & v_{\mathrm{HGU}}(\varphi^{\mathrm{FGu}}, \varphi^{\mathrm{SGy}}, \varphi^{\mathrm{FLc}}) \\ & = p_{\mathrm{HGU}}(\varphi^{\mathrm{FGu}}, \varphi^{\mathrm{SGy}}, \varphi^{\mathrm{FLc}}) \cdot \begin{cases} \dfrac{z}{z + k_{\mathrm{z}}} & \forall\, p_{\mathrm{HGU}} < 0 \\ \dfrac{x}{x + k_{\mathrm{x}}} & \forall\, p_{\mathrm{HGU}} \geq 0 \end{cases} \end{aligned} \tag{71}$$

$$\begin{aligned} & p_{\mathrm{GLY}}(\varphi^{\mathrm{FGu}}, \varphi^{\mathrm{SGy}}, \varphi^{\mathrm{FLc}}) \\ & = \frac{V_{\mathrm{f}}\, \mathrm{m}_{\mathrm{bw}}}{60 \cdot 10^{-3}} \cdot (C_{\mathrm{GLY}}[1] \cdot \mathrm{x}^3 + \mathrm{C}_{\mathrm{GLY}}[2] \cdot x^2 y + C_{\mathrm{GLY}}[3] \cdot x^2 \\ & + C_{\mathrm{GLY}}[4] \cdot x y^2 + C_{\mathrm{GLY}}[5] \cdot x y + C_{\mathrm{GLY}}[6] \cdot x + C_{\mathrm{GLY}}[7] \cdot y^3 \\ & + C_{\mathrm{GLY}}[8] \cdot y^2 + C_{\mathrm{GLY}}[9] \cdot y + C_{\mathrm{GLY}}[10]) \end{aligned} \tag{72}$$

$$\begin{aligned} & v_{\mathrm{GLY}}(\varphi^{\mathrm{FGu}}, \varphi^{\mathrm{SGy}}, \varphi^{\mathrm{FLc}}) \\ & = p_{\mathrm{GLY}}(\varphi^{\mathrm{FGu}}, \varphi^{\mathrm{SGy}}, \varphi^{\mathrm{FLc}}) \cdot \begin{cases} \dfrac{z}{z + k_{\mathrm{z}}} & \forall\, p_{\mathrm{GLY}} < 0 \\ \dfrac{x}{x + k_{\mathrm{x}}} & \forall\, p_{\mathrm{GLY}} \geq 0 \end{cases} \end{aligned} \tag{73}$$

$$\begin{aligned} & v_{\mathrm{GS}}(\varphi^{\mathrm{FGu}}, \varphi^{\mathrm{SGy}}, \varphi^{\mathrm{FLc}}) \\ & = v_{\mathrm{HGU}}(\varphi^{\mathrm{FGu}}, \varphi^{\mathrm{SGy}}, \varphi^{\mathrm{FLc}}) - \mathrm{v}_{\mathrm{GLY}}(\varphi^{\mathrm{FGu}}, \varphi^{\mathrm{SGy}}, \varphi^{\mathrm{FLc}}) \end{aligned} \tag{74}$$

$$\begin{aligned} \frac{\mathrm{d}\, \varphi^{\mathrm{FGu}}}{\mathrm{dt}} & = -\mathrm{v}_{\mathrm{HGU}}(\varphi^{\mathrm{FGu}}, \varphi^{\mathrm{SGy}}, \varphi^{\mathrm{FLc}}) = \hat{\mathrm{c}}^{\mathrm{FGu}}, \\ \frac{\mathrm{d}\, \varphi^{\mathrm{SGy}}}{\mathrm{dt}} & = -\mathrm{v}_{\mathrm{HGU}}(\varphi^{\mathrm{FGu}}, \varphi^{\mathrm{SGy}}, \varphi^{\mathrm{FLc}}) = \hat{\mathrm{c}}^{\mathrm{FGu}}, \\ \frac{\mathrm{d}\, \varphi^{\mathrm{FLc}}}{\mathrm{dt}} & = 2 \cdot \mathrm{v}_{\mathrm{GLY}}(\varphi^{\mathrm{FGu}}, \varphi^{\mathrm{SGy}}, \varphi^{\mathrm{FLc}}) = \hat{\mathrm{c}}^{\mathrm{FLc}}. \end{aligned} \tag{75}$$

References

Ateshian GA (2007) On the theory of reactive mixtures for modeling biological growth. Biomech Model Mechanobiol 6:423–445

Ateshian GA, Costa KD, Azeloglu EU, III BM, Hung CT (2009) Continuum modeling of biological tissue growth by cell division, and alteratin of intracellular osmolytes and extracellular fixed charge density. J Biomech Eng 131(10):101001. doi:10.1115/1.3192138

Babcock M, Cardell J (1974) Hepatic glycogen patterns in fasted and fed rats. Am J Anat 140:299–337

Biot MA (1935) Le probléme de la consolidation des matièeres argileuses sous une charge. Annales de la Societé scientifique de Bruxelles 55:110–113

Biot MA (1941) General theory of three dimensional consolidation. J Appl Phys 12:155–164

Blouin A, Bolender RP, Weibel ER (1977) Distribution of organelles and membranes between hepatocytes and nonhepatocytes in the rat liver parenchyma. A stereological study. J Cell Biol 72(2): 441–455

Bluhm J (2002) Modelling of saturated thermo-elastic porous solids with different phase temperatures. In: Ehlers W, Bluhm J (eds) Porous media: theory, experiments and numerical applications. Springer, Berlin

Bowen RM (1976a) Theory of mixtures. In: Eringen AC (ed) Continuum physics, vol III. Academic Press, New York, pp 1–127

Bowen RM (1976b) Theory of mixtures. In: Eringen AC (ed) Continuum physics. Academic Press, New York

Brown JD, Rosen J, Kim YS, Chang L, Sinanan M, Hannaford B (2003) In-vivo and in-situ compressive properties of porcine abdominal soft tissues. In: Westwood JD, Hoffman HM, Mogel GT, Phillips R, Robb RA, Stredney D (eds) Medicine meets virtual reality 11, vol 94. IOS Press, Amsterdam, pp 26–32

Burt A, Portmann B, Ferrell L (2007) MacSweens pathology of the liver. Elsevier, Churchill Livingstone

Coleman BD, Noll W (1963) The thermodynamics of elastic materials with heat conduction and viscosity. Arch Ration Mech Anal 13:167–178

Corrin B, Aterman K (1968) The pattern of glycogen distribution in the liver. Am J Anat 122:57–72

de Boer R (1996) Highlights in the historical development of the porous media theory: toward a transistent macroscopic theory. Appl Mech Rev 4:201–262

de Boer R (2000) Theory of porous media: highlights in the historical development and current state. Springer, Berlin

Debbaut C, Vierendeels J, Siggers JH, Repetto R, Monbaliu D, Segers P (2014) A 3d porous media liver lobule model: the importance of vascular septa and anisotropic permeability for homogeneous perfusion. Comput Methods Biomech Biomed Eng 17(12):1295–1310

Dirsch O, Madrahimov N, Chaudri N, Deng M, Madrahimova F, Schenk A, Dahmen U (2008) Recovery of liver perfusion after focal outflow obstruction and liver resection. Transplantation 85: 748–756

Ehlers W (2002) Foundations of multiphasic and porous materials. In: Ehlers W, Bluhm J (eds) Porous media: theory, experiments and numerical applications. Springer, Berlin, pp 3–86

Eipper G (1998) Theorie und Numerik finiter elastischer Deformationen in fluidgesättigten Porösen Medien. Dissertation, Bericht Nr. II-1 aus dem Institut für Mechanik (Bauwesen), Universität Stuttgart

Evans DW, Moran EC, Baptista PM, Soker S, Sparks J (2013) Scale-dependent mechanical properties of native and decellularized liver tissue. Biomech Model Mechanobiol 12(3):569–580

Garikipati K, Olberding JE, Narayanan H, Arruda EM, Grosh K, Calve S (2006) Biological remodelling: stationary energy, configurational change, internal variables and dissipation. J Mech Phys Solids 54(7):1493–1515

Gerich J (1993) Control of glycaemia. Baillieres Clin Endocrinol Metab 7(3):551–86

Greve R (2003) Kontinuumsmechanik: Ein Grundkurs. Springer, Berlin

Grytz R, Girkin CA, Libertiaux V, Downs JC (2012a) Perspectives on biomechanical growth and remodeling mechanisms in glaucoma. Mech Res Commun 42:92–106

Grytz R, Sigal IA, Ruberti JW, Meschke G, Downs C (2012b) Lamina cribrosa thickening in early glaucoma predicted by a microstructure motivated growth and remodeling approach. Mech Mater 44:99–109

Hall C (2006) Regulation der hepatischen mikrozirkulation bei schrittweiser resektion im rattenlebermodell. PhD thesis, Medizinische Fakultät der Universität Duisburg-Essen, Zentrum für Chirurgie Klinikum für Allgemeinchirurgie, Viszeral-und Transplantationschirurgie

Hariton I, deBotton G, Gasser TC, Holzapfel GH (2007) Stress-driven collagen fiber remodeling in arterial walls. Biomech Model Mechanobiol 6(3):163–175

Humphrey JD, Rajagopal KR (2002) A constrained mixture model for growth and remodelling of soft tissues. Math. Models Methods Appl Sci 12(3):407–430

Hutter K, Jöhnk K (2004) Continuum methods of physical modeling: continuum mechanics, dimensional analysis, turbulence. Springer, Berlin

Job G, Herrmann F (2006) Chemical potentiala quantity in search of recognition. Eur J Phys 27:353–371

Jungermann K (1986) Functional heterogeneity of periportal and perivenous hepatocytes. Enzyme 35:161–180

Kerdok AE (2006) Characterizing the nonlinear mechanical response of liver to surgical manipulation. PhD thesis, Harvard University, Engineering and Applied Sciences

König M, Bulik S, Holzhütter H (2012) Quantifying the contribution of the liver to glucose homeostasis: a detailed kinetic model of human hepatic glucose metabolism. PLoS Comput Biol 8(6):e1002,577

Kuhl E, Holzapfel GA (2007) A continuum model for remodeling in living structures. J Mater Sci 42:8811–8823

Kuntz E, Kuntz HD (2006) Hepatology: principles and practice. Springer, Berlin

Lai WM, Hou JS, Mow VC (1991) A triphasic theory for the swelling and deformation behaviours of articular cartilage. ASME J Biomech Eng 113:245–258

Lautt WW (2009) Hepatic circulation. University of Manitoba, San Rafael

Lu JF, Hanyga A (2005) Linear dynamic model for porous media saturated by two immiscible fluids. Int J Solids Struct 42:2689–2709

Maass-Moreno R, Rothe CF (1997) Distribution of pressure gradients along hepatic vasculature. Am J Physiol Heart Circ Physiol 272(6):H2826–H2832. http://ajpheart.physiology.org/content/272/6/H2826.full.pdf

MacPhee PJ, Schmidt EE, Groom AC (1995) Intermittence of blood flow in liver sinusoids, studied by high-resolution in vivo microscopy. Am J Physiol Gastrointest Liver Physiol 269(5):G692–G698. http://ajpgi.physiology.org/content/269/5/G692.full.pdf

Millonig G, Friedrich S, Adolf S, Fonouni H, Golriz M, Mehrabi A, Stiefel P, Pschl G, Bchler MW, Seitz HK, Mueller S (2010) Liver stiffness is directly influenced by central venous pressure. J Hepatol 52(2):206–210

Mow VC, Gibbs MC, Lai WM, Zhu WB, Athanasiou KA (1989) Biphasic indentation of articular cartilage-ii. A numerical algorithm and an experimental study. J Biomech 22:853–861

Nava A, Mazza E, Furrer M, Villiger P, Reinhart WH (2008) In vivo mechanical characterization of human liver. Med Image Anal 12(2):203–216

Nuttal FQ, Ngo A, Gannon MC (2008) Regulation of hepatic glucose production and the role of gluconeogenesis in humans: is the rate of gluconeogenesis constant? Diabetes Metab Res Rev 24:438–458

Pierce DM, Ricken T, Holzapfel GA (2013a) A hyperelastic biphasic fibre-reinforced model of articular cartilage considering distributed collagen fibre orientations: continuum basis, computational aspects and applications. Comput Methods Biomech Biomed Eng 16(12):1344–1361

Pierce DM, Ricken T, Holzapfel GA (2013b) Modeling sample/patient-specific structural and diffusional responses of cartilage using DT-MRI. Int J Numer Methods Biomed Eng 29(8):807–821

Radziuk J, Pye S (2001) Hepatic glucose uptake, gluconeogenesis and the regulation of glycogen synthesis. Diabetes Metab Res Rev 17:250–272

Ricken T (2002) Kapillarität in porösen medien—theoretische untersuchung und numerische simulation. PhD thesis, Dissertation, Shaker Verlag, Aachen

Ricken T, Bluhm J (2009) Evolutional growth and remodeling in multiphase living tissue. Comput Mater Sci 45(3):806–811

Ricken T, Bluhm J (2010) Remodeling and growth of living tissue: a multiphase theory. Arch Appl Mech 80(5):453–465

Ricken T, de Boer R (2003) Multiphase flow in a capillary porous medium. Comput Mater Sci 28:704–713

Ricken T, Dahmen U, Dirsch O (2010) A biphasic model for sinusoidal liver perfusion remodeling after outflow obstruction. Biomech Model Mechanobiol 9:435–450

Saitoh Y, Terada N, Saitoh S, Ohno N, Fujii Y, Ohno S (2010) Histochemical approach of cryobiopsy for glycogen distribution in living mouse livers under fasting and local circulation loss conditions. Histochem Cell Biol 133(2):229–239

Samur E, Sedef M, Basdogan C, Avtan L, Duzgun O (2005) A robotic indenter for minimally invasive characterization of soft tissues. In: International congress series, CARS 2005: computer assisted radiology and surgery proceedings of the 19th international congress and exhibition, vol 1281, no 0, pp 713–718

Sasse D (1975) Dynamics of liver glycogen: the topochemistry of glycogen synthesis, glycogen content and glycogenolysis under the experimental conditions of glycogen accumulation and depletion. Histochemistry 45:237–254

Schwartz JM, Denninger M, Rancourt D, Moisan C, Laurendeau D (2005) Modelling liver tissue properties using a non-linear visco-elastic model for surgery simulation. Med Image Anal 9(2):103–112

Siggers JH, Leungchavaphongse K, Ho CH, Repetto R (2014) Mathematical model of blood and interstitial flow and lymph production in the liver. Biomec Model Mechanobiol 13(2):363–378

Stanhope KL, Griffen SC, Bair BR, Swarbrick MM, Keim NL, Havel PJ (2008) Twenty-four-hour endocrine and metabolic profiles following consumption of high-fructose corn syrup-, sucrose-, fructose-, and glucose-sweetened beverages with meals. Am J Clin Nutr 87:1194–1203

Teutsch HF (2005) The modular microarchitecture of human liver. Hepatology 42(2):317–325

Teutsch HF, Schuerfeld D, Groezinger E (1999) Three-dimensional reconstruction of parenchymal units in the liver of the rat. Hepatology 29(2):494–505

Truesdell C (1984) Thermodynamics of diffusion. In: Truesdell C (ed) Rational thermodynamics. Springer, New York, pp 219–236

Truesdell C, Toupin R (1960) The classical field theory. In: Flügge S (ed) Handbuch der Physik, vol 3/1. Springer, Berlin

Valentin A, Humphrey JD, Holzapfel GA (2013) A finite element-based constrained mixture implementation for arterial growth, remodeling, and adaptation: theory and numerical verification. Int J Numer Methods Biomed Eng 29(8):822–849

Villeneuve JP, Dagenais PM, Huet P, Roy A, Lapointe R, Marleau D (1996) The hepatic microcirculation in the isolated perfused human liver. Hepatology 23(1):24–31

Wahren J, Ekberg K (2007) Splanchnic regulation of glucose production. Annu Rev Nutr 27:329–345

Walpole J, Papin J, Peirce S (2013) Multiscale computational models of complex biological systems. Ann Rev Biomed Eng 15:137–154

Warren A, Chaberek S, Ostrowski K, Cogger VC, Hilmer SN, McCuskey RS, Fraser R, Le Couteur DG (2008) Effects of old age on vascular complexity and dispersion of the hepatic sinusoidal network. Microcirculation 15(3):191–202

Werner D, Ricken T, Dahmen U, Dirsch O (2012) A biphasic fem model for the microperfusion in liver lobules. PAMM 12:89–90

Yuen K, McDaniel P, Riddle M (2012) Twenty-four-hour profiles of plasma glucose, insulin, c-peptide and free fatty acid in subjects with varying degrees of glucose tolerance following short-term, medium-dose prednisone (20 mg/day) treatment: evidence for differing effects on insulin secretion and action. Clin Endocrinol 77:224–232